AGU PUBLICATIONS

Tectonics

RESEARCH ARTICLE
10.1002/2017TC004578

Key Points:
- A novel approach to restore paleomagnetic data from deformed igneous rocks is described
- New paleomagnetic and magnetic fabric data from Jurassic gabbros of NW Africa are provided
- This study allows a better and more complete constraint of the deformational history of the central High Atlas

Supporting Information:
- Supporting Information S1
- Table S1
- Table S2
- Table S3
- Table S4
- Table S5
- Table S6

Correspondence to:
P. Calvín,
calvinballester@gmail.com

Citation:
Calvín, P., Ruiz-Martínez, V. C., Villalaín, J. J., Casas-Sainz, A. M., & Moussaid, B. (2017). Emplacement and deformation of Mesozoic gabbros of the High Atlas (Morocco): Paleomagnetism and magnetic fabrics. *Tectonics*, *36*, 3012–3037. https://doi.org/10.1002/2017TC004578

Received 22 MAR 2017
Accepted 20 NOV 2017
Accepted article online 24 NOV 2017
Published online 13 DEC 2017

Emplacement and Deformation of Mesozoic Gabbros of the High Atlas (Morocco): Paleomagnetism and Magnetic Fabrics

P. Calvín[1], V. C. Ruiz-Martínez[2], J. J. Villalaín[1], A. M. Casas-Sainz[3], and B. Moussaid[4]

[1]Departamento de Física, Universidad de Burgos, Burgos, Spain, [2]Departamento de Física de la Tierra, Astronomía y Astrofísica, Universidad Complutense de Madrid, Madrid, Spain, [3]Geotransfer, IUCA, Universidad de Zaragoza, Zaragoza, Spain, [4]Lab. «BGIM», Ecole Normale Supérieure, Université Hassan II, Casablanca, Morocco

Abstract A paleomagnetic and magnetic fabric study is performed in Upper Jurassic gabbros of the central High Atlas (Morocco). These gabbros were emplaced in the core of preexisting structures developed during the extensional stage and linked to basement faults. These structures were reactivated as anticlines during the Cenozoic compressional inversion. Gabbros from 19 out of the 33 sampled sites show a stable characteristic magnetization, carried by magnetite, which has been interpreted as a primary component. This component shows an important dispersion due to postemplacement tectonic movements. The absence of paleoposition markers in these igneous rocks precludes direct restorations. A novel approach analyzing the orientation of the primary magnetization is used here to restore the magmatic bodies and to understand the deformational history recorded by these rocks. Paleomagnetic vectors are distributed along small circles with horizontal axes, indicating horizontal axis rotations of the gabbro bodies. These rotations are higher when the ratio between shales and gabbros in the core of the anticlines increases. Due to the uncertainties inherent to this work (the igneous bodies recording strong rotations), interpretations must be qualitative. The magnetic fabric is carried by ferromagnetic (s.s.) minerals mimicking the magmatic fabric. Anisotropy of magnetic susceptibility (AMS) axes, using the rotation routine inferred from paleomagnetic results, result in more tightly clustered magnetic lineations, which also become horizontal and are considered in terms of magma flow trend during its emplacement: NW-SE (parallel to the general extensional direction) in the western sector and NE-SW (parallel to the main faults) in the easternmost structures.

1. Introduction

Paleomagnetism has been extensively applied in gabbros and other related mafic rocks because the primary, stable characteristic magnetization (Denyszyn et al., 2013; Feinberg et al., 2005; Renne et al., 2002) carried by these rocks can be complemented with reliable absolute dating. Different studies have been focused on obtaining paleopoles (Brown & McEnroe, 2015; Denyszyn et al., 2013; Dunlop et al., 1985; Evans & McElhinny, 1966; McEnroe, 1996; Osete et al., 1997; Van der Voo, 1967, 1969 among others), paleointensities (Granot et al., 2007; Muxworthy et al., 2013), and magnetic properties characterizing the stability of the magnetic remanence (Usui & Yamazaki, 2010). In the last years, detailed magnetic studies have targeted on magnetite included within silicate crystals (mainly pyroxene and plagioclase), generated during the solidification of magma and preserving the primary magnetization acquired when magnetite is cooled below its Curie temperature (Evans et al., 1968; Feinberg et al., 2005, 2006; Muxworthy & Evans, 2013; Renne et al., 2002; Usui et al., 2014; Wenk et al., 2011).

Magnetic fabrics have also been analyzed in order to explore in a quick and reliable manner the petrofabric of plutonic rocks for determining (i) the strain regime at the time of magma emplacement or during subsequent stages after magma solidification or (ii) the flow pattern in magmatic chambers (Archanjo et al., 2012; Bouchez, 1997, 2000; Bouchez & Gleizes, 1995; Gil et al., 2002; McNulty et al., 2000; Román-Berdiel et al., 2004, and references therein). Petrofabric and magnetomineralogic studies include typically room temperature anisotropy of the magnetic susceptibility (RT-AMS=, low-temperature anisotropy of the magnetic susceptibility (LT-AMS), anisotropy of the anhysteretic remanent magnetization (AARM), and anisotropy of the isothermal remanent magnetization (AIRM). The combined used of these techniques supports the interpretation of magnetic fabrics (Izquierdo-Llavall et al., 2012; Oliva-Urcia et al., 2012; Schöpa et al., 2015; Usui et al., 2006, and references therein).

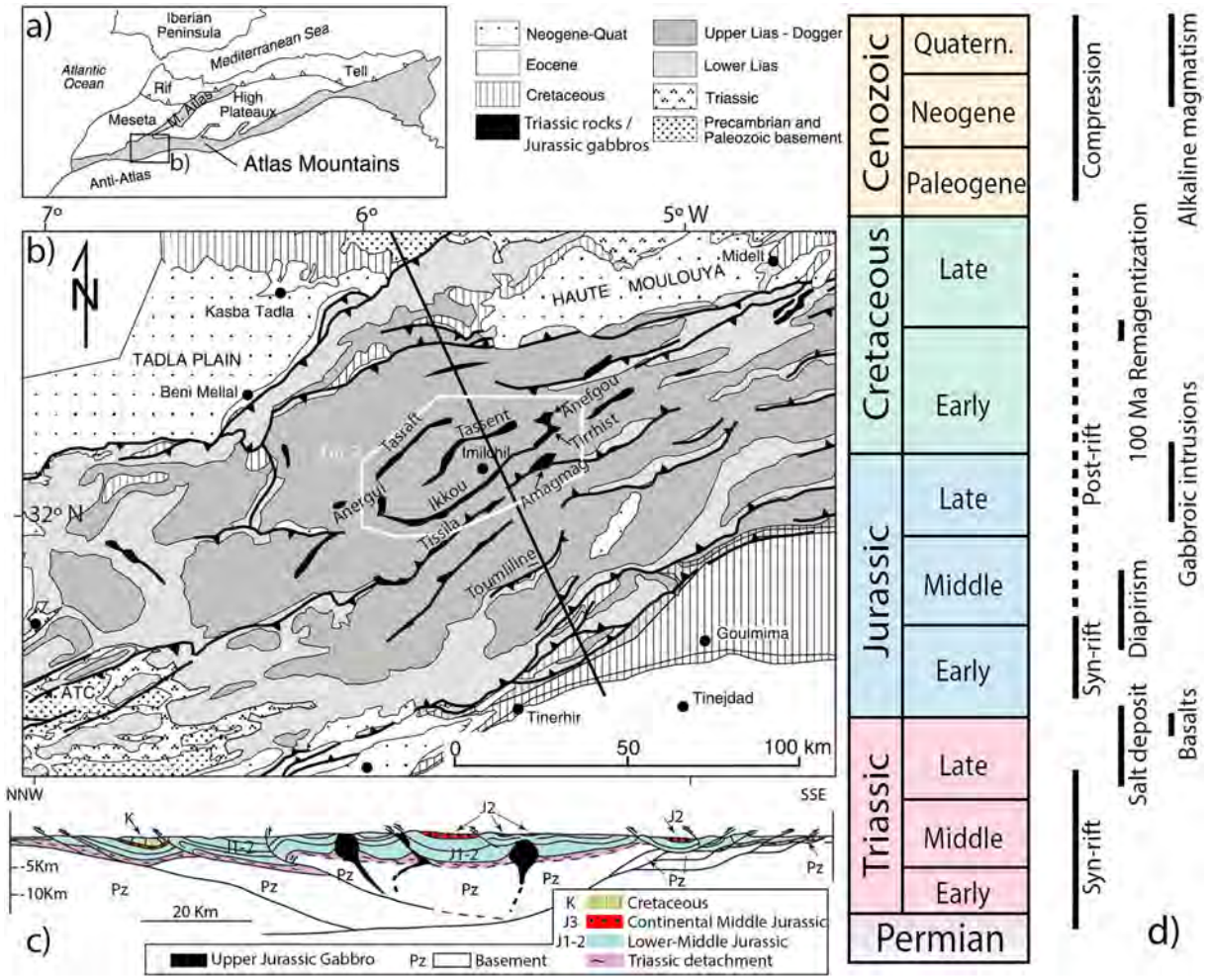

Figure 1. (a) Location sketch map of the Atlas Mountains in the Western Mediterranean framework and (b) geological map of the central High Atlas showing the position of the study area (Figure 2) and the main structures of the region. (c) Geological cross section of the central High Atlas showing the Jurassic gabbro intrusions. Figures 1a and 1b were modified from Teixell et al. (2003), and Figure 1c was modified from Poisson et al. (1998). (d) Simplified temporal evolution of the main geological events occurred in the CHA.

In spite of their spectacular outcrops, the gabbros of the central High Atlas (CHA) have not been yet explored from the paleomagnetic point of view, apart from a pioneering work in the early seventies (Hailwood & Mitchell, 1971).

The Atlas System (Figure 1a) has been classically considered as an intracontinental chain, resulting from the Cenozoic inversion of Mesozoic extensional basins (Frizon de Lamotte et al., 2008; Mattauer et al., 1977, and references therein). Its main structural features are tight anticlines (named classically as "ridges" in the literature) with steeply dipping limbs limiting wide, gentle synclines (Figure 1b). In the core of some of these ridges, Upper Jurassic gabbros crop out. Changes in the general trend of the structures, from ENE-WSW to NE-SW, define sigmoidal shapes in map view (e.g., Tassent ridge, Figures 1b and 2). This fact has generated controversies about the timing and mechanism of formation of the anticlines. The three main mechanisms proposed are (i) superposition of different tectonic phases with different stress axes (de Sitter, 1952), (ii) sinistral transpression during the Jurassic (Laville & Piqué, 1992), and (iii) tectonic control from inherited extensional faults (Beauchamp, 2004). In the last years, further studies have helped to clarify the origin of the ridges. Ettaki et al. (2007), Michard et al. (2011), and Saura et al. (2014) evidenced the occurrence of an early diapirism during the Jurassic that individualized sedimentary depocenters between narrow thresholds (the present-day ridges). By means of detailed paleomagnetic studies performed in Jurassic remagnetized limestones at the limbs of the anticlines, Torres-López et al. (2016) demonstrated that these anticlines were already structured before the Late Cretaceous. Regarding the superposition of different

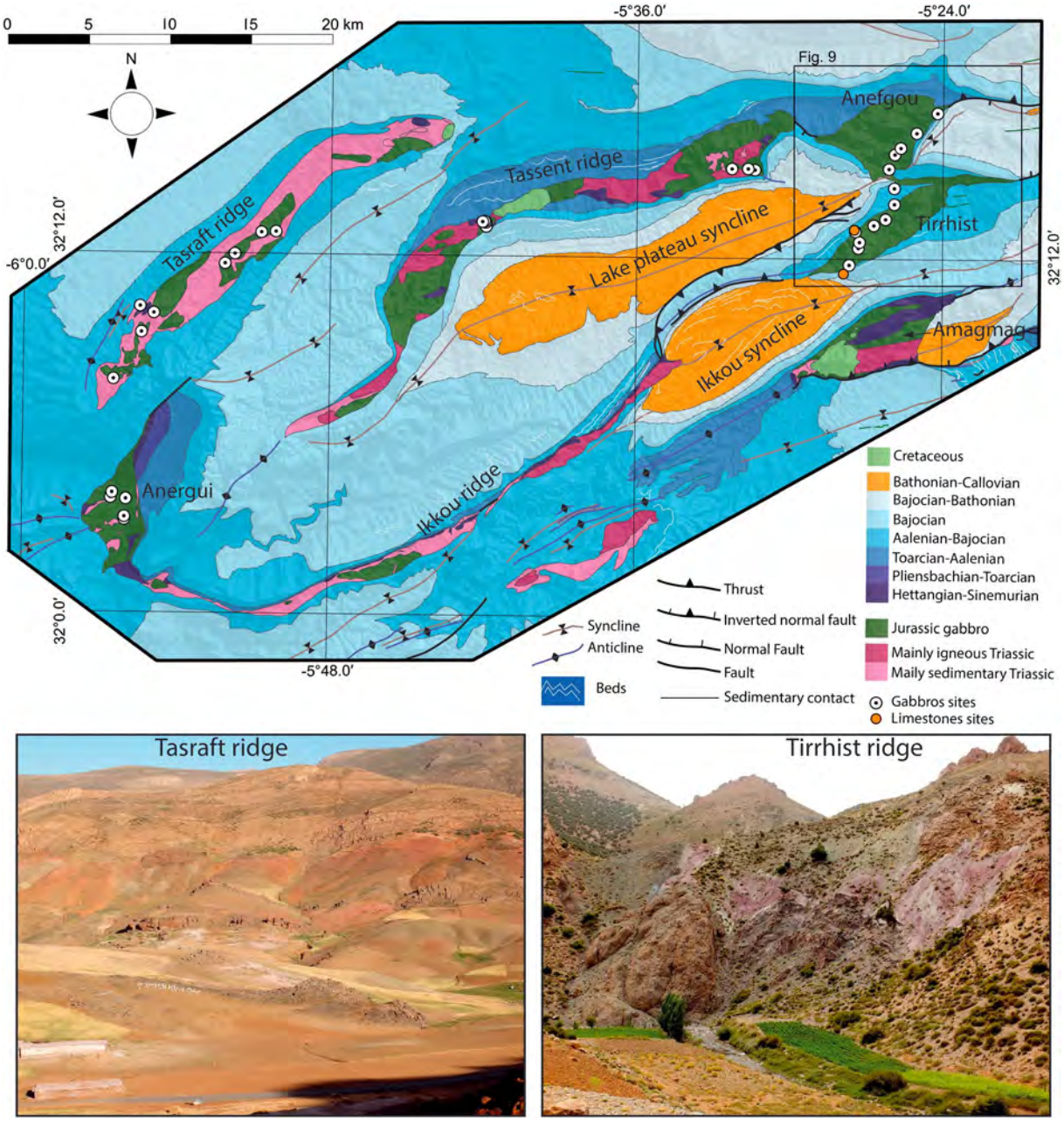

Figure 2. Detailed geological map of the study area showing the gabbro outcrops and the paleomagnetic sites. Datum WGS84 (EPSG: 4326). Pictures of the general outcrops in Tasraft and Tirrhist ridges. The Tasraft picture shows in the foreground the core of the ridge, with the gabbros (the dark rocks in the middle of the picture) and the Triassic shales and basalts (with reddish and greenish tones, respectively); in the background appears the Jurassic limestones. In the Tirrhist picture can be observed the tectonic relationship between the gabbros (the dark rocks in the middle of the picture), the Triassic shales, and the Jurassic limestones.

sets of folds during the Cenozoic compression, Moussaid et al. (2015) showed through a paleomagnetic study that the curvature of the Aït Attab syncline is primary, probably related to the orientation of Mesozoic extensional structures. Michard et al. (2011) indicate the presence of a late diapiric phase (Cenozoic) affecting the core of the anticlines.

In summary, the CHA ridges are structures inherited from the Mesozoic extensional stage, initially formed as straight, long diapirs (salt walls) and conditioned by the structural pattern of the basement (Charrière, 1990; Mattauer et al., 1977). These salt walls acted as sedimentary highs between Jurassic sedimentary depocenters (Ettaki et al., 2007; Saura et al., 2014), and some of these anticlines already presented steeply dipping limbs during the Cenomanian age (Torres-López et al., 2016).

In this paper, paleomagnetic, magnetic fabrics, and rock magnetism studies are presented in order to decipher the processes occurring at the core of the ridges of the CHA. On one hand, (1) directional analysis of paleomagnetic vectors can give information about the postemplacement rotations of the igneous bodies. On the other hand (2), magnetic fabrics can allow to characterize the tectonic regime under which the gabbros were emplaced and/or the processes related to magma ascent.

2. The Ridges of the Central High Atlas

2.1. Geological Setting

Detailed syntheses about the Mesozoic evolution of the CHA can be found in Frizon de Lamotte et al. (2008), Ibouh et al. (2014), and Saura et al. (2014, and references therein). Mesozoic sedimentation began with Triassic continental clastic sediments and evaporites during the first rifting stage, in a horst-graben system controlled by NE-SW normal faults. These series are topped by Triassic-Jurassic basalts. During the second rifting stage (Early-Middle Jurassic) faults were reactivated, and more than 5,000 m of Jurassic marine sediments accumulated in the depocenters until the end of Bajocian times (Frizon de Lamotte et al., 2008, and references therein). The NW-SE extension was oblique to the main trend of the CHA, and NE-SW normal faults were generated in addition to ENE-WSW faults. Diapiric processes began at this stage, favored by extensional tectonics. Salt walls formed at the footwall of normal faults, bounding minibasins (Saura et al., 2014). The Bathonian is characterized by lacustrine and fluvial red beds. During the Late Jurassic-Early Cretaceous the CHA eventually emerged (Charrière & Haddoumi, 2016). Cretaceous sedimentation is characterized by red beds followed by expansive tabular limestones corresponding with postrift sediments.

During the Late Jurassic an extensive magmatic event, characterized by mafic intrusions (troctolites and gabbros) during the main phase, and intermediate (diorites and monzodiorites) and felsic rocks (syenites), resulting mainly from fractional crystallization processes (Zayane et al., 2002), occurred. Subsequently, more felsic rocks intruded the mafic rocks. In this study, dealing with gabbros s.s. and troctolites, the "gabbro" term refers to the whole set of intrusive mafic rocks. The cooling ages of these rocks were dated in the Tassent ridge with K-Ar in biotite at 160 ± 3 Ma to 152 ± 3 Ma (Hailwood & Mitchell, 1971) and in the Anefgou ridge with Ar-Ar in biotite at 151.3 ± 0.5 Ma to 146 ± 0.5 Ma (Armando, 1999). Moreover, mafic dikes intruded during the Early Cretaceous, between 119 ± 3 Ma and 134 ± 3 Ma according to ages obtained from K-Ar in biotite (Hailwood & Mitchell, 1971).

Late Cretaceous-Cenozoic Alpine compression was relatively weak in the Atlas, with a 15% to 24% of shortening in the CHA (Teixell et al., 2003). The deformation is accommodated by the squeezing of previous extensional and diapiric structures, giving the current ridges (e.g., Torres-López et al., 2014) and double vergence angular folds with different degree of cleavage development (Calvín et al., 2017).

2.2. Structure of the Studied Ridges

Gabbros crop out in five ridges (Figures 1 and 2) whose structure can be summarized, from west to east, as follows:

The Anergui ridge shows a core of Triassic sedimentary rocks and Jurassic gabbros. It shows a main NNE-SSW trend, which turns to ESE-WNW toward the south, joining the Ikkou ridge. The structure of its limbs shows different patterns. Toward the east, Lower Jurassic limestones dip moderately toward the SE, connecting with the SE limb of the Tasraft anticline. In the western limb, E-W trending, north vergent folds affect the Middle Jurassic rocks.

The Tasraft ridge is a NE-SW trending, 25 km long anticline whose core is formed by Triassic rocks including several gabbro outcrops. Its limbs are defined by Middle Jurassic limestones with moderate to steep dips close to its core, rapidly decreasing to subhorizontal with increasing distance to the core. The contacts between the shales at its core and the limestones at its limbs are mainly diapiric.

The Tassent ridge is a 45 km long antiform, whose trend changes from ENE-WSW to NE-SW. Its core is dominated by igneous rocks, with scarce, isolated outcrops of Triassic shales. The width of Triassic outcrops varies along strike, from less than 1 km along the eastern to 3.5 km along the western sampled sections, the wider outcrop coinciding with the major exposures of igneous rocks. Along the fold limbs the Jurassic limestones

are faulted against the Upper Triassic shales at the core, showing steep dips that decrease with the distance to the core.

The Anefgou and Tirrhist ridges are the eastern continuations of the Tassent and Ikkou ridges, respectively. Unlike their western counterparts, these structures are much shorter along trend. Tirrhist is around 17 km long and 5 km wide, and Anefgou is around 10 km long and 4 km wide. Their general trend is ENE-WSW, although in detail they are defined by three limbs with different strikes, enclosing triangular areas. The two outcrops of gabbro at their cores have a rough sigmoidal shape in map view. The cores of both anticlines show large amounts of igneous rocks (mainly gabbros intruded by intermediate to acid igneous rocks) and a few outcrops of Triassic shales. The limbs are constituted by Middle Jurassic limestones.

In summary, Tasraft and Tassent are long structures with varying trends (NE-SW and ENE-WSW). In their cores an apparent chaotic mix of Triassic gypsiferous red shales, Triassic basalts, slivers of Liassic carbonates, and Middle-Upper Jurassic plutonic igneous rocks crops out (Figure 2). Conversely, the Tirrhist, Anefgou, and Anergui massifs (Figure 2) are short structures, whose cores are largely occupied by gabbro outcrops with minor presence of Triassic shales. Independently of the amount of gabbro and according to outcrop observations (Figures 1e and 1f), common points between the different ridge cores are the heterogeneity of outcrops of igneous rocks, showing different alteration degrees, the strong Cenozoic tectonic imprint resulting in faults between rigid blocks, and the scarcity of primary contacts between the gabbros and the host rocks.

3. Previous Paleomagnetic Works in the Study Area

In addition to Hailwood and Mitchell (1971) pioneering work in the Jurassic igneous rocks (whose aim was to obtain Jurassic paleomagnetic poles from South Morocco), paleomagnetic work has been focused on both sedimentary and igneous rocks from the CHA. Torres-López et al. (2014) presented a paleomagnetic and rock magnetism work on the Jurassic limestones. These authors found a regional, pervasive, and widespread chemical remagnetization (CRM), which affects to all the Jurassic limestones of the CHA. The interpreted age for this remagnetization is circa 100 Ma, by comparison between its orientation and the global apparent polar wander path (GAPWP) in African coordinates. Torres-López et al. (2016) used this remagnetization to restore the actual geometry of three ridges (Tassent and Tasraft ridges between them) to the remagnetization time, and Calvín et al. (2017) also restored folds with axial-plane cleavage to the preremagnetization stage, interpreting a Cenozoic age for cleavage formation.

Other paleomagnetic work is related to Mesozoic magmatic events such as the Early Cretaceous dikes and their relationship with the host rocks (Villalaín, Casas-Sainz, & Soto, 2016; Villalaín, Ruiz, et al., 2016). These authors analyzed the relationship between dikes, limestones, and the circa 100 Ma remagnetization described by Torres-López et al. (2014), by means of baked contact tests. Limestones affected by contact metamorphism show two remagnetization vectors: one component is carried by pyrrhotite, with a paleomagnetic direction similar to the dikes and consistent with the age of the igneous rocks (Late Jurassic-Early Cretaceous). The other component is carried by magnetite and presents a more northward direction, corresponding to the circa 100 Ma regional remagnetization. Therefore, and according to the above cited work, limestones are capable of recording two remagnetizations, whereas the igneous rocks are not affected by the regional remagnetization, carrying only the primary component.

4. Methodology

A total of 33 sites was sampled (Figure 2) along five structures. Eight cores were taken at each site, with a portable gas-powered drill. Orientations were measured with a magnetic compass (and a solar one when possible). The sampling was conditioned by the quality of the gabbro outcrops and the neighboring roads. Furthermore, two limestone sites were sampled in two of the three limbs of the Tirrhist anticline, close to gabbro sites, in order to restore the limbs of the structure to the age of the magnetization in the way shown by Villalaín, Casas-Sainz, and Soto (2016), Villalaín, Ruiz, et al. (2016), and Torres-López et al. (2016).

Paleomagnetic analyses were conducted on 303 specimens using a 2G cryogenic magnetometer, which integrates alternating field (AF) coils, at the Paleomagnetic Laboratory of the University of Burgos (Spain). After AF and thermal (Th) pilot demagnetization, 9 sites were demagnetized by AF and 24 by Th according to the behavior of the different samples in order to isolate the paleomagnetic components. Nevertheless,

most of the sites showed similar behavior under both demagnetization techniques (see section 5.1). Stepwise thermal demagnetization from room temperature up to 580–600°C was conducted using a TD48-DC thermal demagnetizer in 10 to 17 steps and a stepwise AF demagnetization from 0 mT to 100 mT. Magnetic susceptibility was monitored during thermal demagnetization in order to detect mineralogical changes. Paleomagnetic directional components were calculated by principal component analysis (orientation and maximum angular deviation error (MAD) of the component; Kirschvink, 1980) on orthogonal demagnetization diagrams using Remasoft 3.0 software (Chadima & Hrouda, 2006). Then, the site mean directions and related statistical parameters were calculated (Fisher, 1953).

The internal structure of the gabbro bodies was studied by petrofabric and magnetic fabric analysis in order to understand the meaning of the magnetic fabrics (by comparison with the petrofabric) and to avoid possible problems with anomalous fabrics (Potter & Stephenson, 1988; Schöbel & de Wall, 2014 for review). Anisotropy of magnetic susceptibility at room temperature (RT-AMS) was measured using a KLY4 Kappabridge (Agico). Between 6 and 23 specimens per site were measured, with a total of 434 measured specimens. The magnitudes and orientations of the three axes (k_1, k_2, and k_3) of the AMS ellipsoid were obtained according to the statistical procedure based on Jelínek (1978). The relationship between the magnetic axes was analyzed by means of the normalized parameters (Jelinek, 1981) *Pj* (corrected anisotropy degree) and *T* (shape parameter), which show the eccentricity and shape of the ellipsoid (from −1, prolate, to 1, oblate), respectively.

In addition, the AMS at low temperature (LT-AMS) was measured in order to discriminate the contribution of the paramagnetic phases (Oliva-Urcia et al., 2011, and references therein), because under pure paramagnetic behavior and following the Curie-Weiss law, the bulk susceptibility shows an increase of about 3.8 times of susceptibility at 77 K (e.g., Lüneburg et al., 1999; Morrish, 1965). Sixteen specimens from nine sites were measured after being immersed in liquid nitrogen (at 77 K) during 45 min before the initial measurement and 15 min before each measured position.

The anisotropy of the anhysteretic remanent magnetization (AARM) (McCabe et al., 1985) was used to obtain the magnetic fabric of the ferromagnetic s.s. minerals with coercivities below 90 mT. Sixteen specimens from 15 sites were measured following a standard protocol. (i) After demagnetization of the sample with an AF peak of 100 mT, (ii) an ARM is imparted in a decreasing AF with a peak of 90 mT and a coaxial direct field of 50 μT, along a specific axis of the specimen; (iii) then, the remanence along this axis is measured in a cryogenic magnetometer and (iv) the ARM is removed with an AF peak of 100 mT along the same axis. The operation is repeated imparting and measuring the ARM along nine different axes (Girdler, 1961) to calculate the AARM magnetic tensor.

The foliation observable at sample scale and defined by tabular crystals (mainly plagioclase) was measured and compared with the magnetic fabric. Thin sections were made perpendicular to the magnetic foliation and observed under a polarizing microscope. By doing so, it was possible to compare magnetic and petrological fabric of 18 samples.

Regarding the magnetic mineralogy, several rock magnetic experiments were performed in representative samples of each site. Acquisition of isothermal remanent magnetization (IRM), temperature-dependent induced magnetization and backfield curves, and hysteresis loops were performed by means of a magnetic variable field translation balance. Hysteresis parameters of silicate crystal (plagioclase, pyroxene, and amphibole) were measured using the Alternating Gradient Force Magnetometer of the Institute for Rock Magnetism (University of Minnesota, USA). In addition, temperature-dependent susceptibility curves were performed using a KLY4 Kappabridge susceptometer with a CS3 furnace (temperature range between 25 and 710°C) and a CSL cryostat (from −195 to 0°C). Susceptibility curves were measured under argon atmosphere in order to avoid mineral oxidations. With the exception of the measurements on silicate crystals, the rock magnetic measurements were performed in the Paleomagnetic Laboratory of the University of Burgos (Spain).

5. Results

5.1. NRM and Paleomagnetic Components

Site mean intensities of natural remanent magnetization (NRM) are in the order of 200–500 mA/m, with extreme values of 2,500 mA/m (around 16,000 mA/m in TIR4, probably affected by lightning

AGU Tectonics

10.1002/2017TC004578

Table 1

Remanent Magnetization Parameters for the H Component in the Gabbros and for the Remagnetization Component in Limestone Sites (CTR-6 and CTR-9)

		Coordinates (WGS84)							In situ directions				Corrected to Jurassic direction (320/40)			Rotation registered	
Zone	Site	Longitude	Latitude	Type	n	N	NRM (mA/m)	e	*D*	*I*	*K*	α_{95}	*D*	*I*	Rotation axis	Amount	Sense
Anergui	ANE1	5° 55′ 59.10″ W	32° 03′ 5.70″ N	B-A	8	8	131	37	301.6	15.2	91.4	5.8	320.6	39.6	165	42	CCW
Anergui	ANE2	5° 55′ 59.10″ W	32° 03′ 11.28″ N	B-A	8	8	485	175	295.9	39.5	274.8	3.3	319.7	39.6	128	28	CCW
Anergui	ANE3	5° 56′ 31.44″ W	32° 03′ 49.32″ N	A	7	8	291	116	273.8	−10.5	86.2	6.5	321.1	39.7	133	116	CCW
Anergui	ANE4	5° 56′ 28.26″ W	32° 03′ 59.16″ N	A	8	8	598	102	288.6	5	338.1	3	319.7	38.9	148	72	CCW
Anergui	ANE5	5° 55′ 55.74″ W	32° 03′ 46.86″ N	C-B	0	8	336	149									
Anefgou	ANF1	5° 26′ 7.68″ W	32° 15′ 0.36″ N	C	0	8	211	172									
Anefgou	ANF2	5° 25′ 54.12″ W	32° 15′ 29.52″ N	B	8	8	464	272	289.2	46.3	29.7	10.3	308.1	34	90	35	CCW
Anefgou	ANF3	5° 24′ 13.98″ W	32° 16′ 52.80″ N	C	0	8	462	342									
Anefgou	ANF4	5° 25′ 2.940 W	32° 16′ 12.66″ N	C	0	8	394	406									
Anefgou	ANF5	5° 25′ 40.20″ W	32° 15′ 42.66″ N	B	6	8	170	166	300.1	51.3	46.3	10	316.6	38	90	21	CCW
Tirrhist	IC33	5° 27′ 40.08″ W	32° 11′ 48.12″ N	B	6	8	488	52	312.2	26	49.7	9.6	308	32.5	90	10	CW
Tirrhist	IC34	5° 26′ 42.54″ W	32° 13′ 7.62″ N	A	8	8	570	92	305	44.6	207.9	3.9	312.1	37.5	90	11	CCW
Tirrhist	IC35	5° 27′ 25.92″ W	32° 12′ 55.26″ N	B	7	8	717	536	264.7	48.4	231.9	4	307.6	32.1	90	49	CCW
Tirrhist	IC36	5° 27′ 16.08″ W	32° 12′ 33.96″ N	A	8	8	1058	1033	250.2	47.6	65.5	6.9	308	36.4	90	57	CCW
Tirrhist	TIR1	5° 25′ 54.48″ W	32° 13′ 49.80″ N	A-B	8	8	314	108	266.3	49.9	134.6	4.8	308.5	34.8	90	45	CCW
Tirrhist	TIR2	5° 26′ 14.94″ W	32° 13′ 20.04″ N	C	0	8	748	367									
Tirrhist	TIR3	5° 25′ 54.84″ W	32° 14′ 21.84″ N	C	0	8	2.23	2									
Tirrhist	TIR4	5° 27′ 18.66″ W	32° 12′ 21.96″ N	C-B	0	8	16589	13150									
Tasraft	TRF1	5° 56′ 28.08″ W	32° 07′ 46.68″ N	C	0	8	290	402									
Tasraft	TRF2	5° 55′ 23.40″ W	32° 09′ 20.70″ N	C-B	5	8	2407	1578	344.1	24.8	217.4	5.2	319.2	39.8	131	40	CW
Tasraft	TRF3	5° 54′ 54.72″ W	32° 09′ 59.22″ N	C	0	8	764	504									
Tasraft	TRF4	5° 55′ 26.94″ W	32° 10′ 12.72″ N	C	0	8	1587	382									
Tasraft	TRF5	5° 52′ 8.46″ W	32° 11′ 39.78″ N	A	8	8	412	200	121.3	−34	330.7	3.1	319.4	39.9	40	174	CCW
Tasraft	TRF6	5° 51′ 45.54″ W	32° 11′ 59.28″ N	A	8	8	84.3	29	107.2	10.4	87.4	6	318.8	39.9	31	128	CCW
Tasraft	TRF7	5° 50′ 43.56″ W	32° 12′ 42.78″ N	C	0	8	92.3	23									
Tasraft	TRF8	5° 50′ 9.42″ W	32° 12′ 44.58″ N	C-B	0	8	372	115									
Tassent E	TSS1	5° 31′ 23.34″ W	32° 14′ 56.70″ N	C	0	8	335	656									
Tassent E	TSS2	5° 31′ 39.42″ W	32° 14′ 58.92″ N	B-A	8	8	356	64	68.7	−32.2	84.9	6	140.7	−38.9	108	79	CCW
Tassent E	TSS3	5° 32′ 17.46″ W	32° 14′ 58.62″ N	A	7	8	430	223	94.1	47	45.3	9.1	140.1	38.6	108	159	CCW
Tassent W	IC8	5° 41′ 54.84″ W	32° 12′ 58.80″ N	C	0	8	1.817	1									
Tassent W	IC9	5° 41′ 55.98″ W	32° 13′ 7.08″ N	A-B	8	8	86.1	21	316.1	−3.5	27.5	10.7	149.8	−41.2	52	135	CCW
Tassent W	IC10	5° 41′ 58.74″ W	32° 13′ 9.36″ N	A	8	8	164	30	340	−20	54.1	7.6	131.3	−38.5	57	120	CCW
Tassent W	IC30	5° 42′ 3.42″ W	32° 13′ 8.40″ N	A	8	8	143	23	339.5	−16.1	42.3	8.6	131.9	−39.7	57	123	CCW
													Corrected to remagnetization direction (336.4/29.2)				
Limb of Tirrhist	CTR-6	5° 27′ 53.22″ W	32° 11′ 30.54″ N	-	8	8	24.7	34	330.3	44.4	89.5	5.9	334.3	44.4	81	17	CCW
	CTR-9	5° 27′ 28.38″ W	32° 12′ 58.62″ N	-	7	8	13.22	11	6.6	70.1	65.2	7.5	342.5	27.3	59	45	CCW

Note. Amount and sense of rotation (looking to the azimuth of the rotation axis) registered for the limestones and the gabbros since the acquisition of the paleomagnetic component are also indicated (data for Tasraft zone are restored according to option 1, see section 6.1 for further explanations). *n*: number of samples in which the *H* component was calculated. *N*: number of demagnetized samples per site. NRM: magnetization of the NRM. *e*: standard deviation of NRM. *D*: magnetization declination. *I*: magnetization inclination. *k* and α_{95}, Fisher statistical parameters (Fisher, 1953); CW: clockwise; CCW: counterclockwise.

remagnetization) and 2 mA/m (Table 1). Magnetic susceptibility values range between 0.3×10^{-3} and 165×10^{-3} SI, with a mean value of 18×10^{-3} SI (Table 2).

The NRM shows different behaviors, in both AF and Th demagnetization diagrams, attending to the observed directional components (named A, B and C, Figure 3). Behavior A is mainly unidirectional (Figure 3a), characterized by a high-temperature component (*H* component) that is destroyed between 500 and 565°C; it is the carrier of 90% of the magnetization. When submitted to AF demagnetization, samples of this group show two different behaviors: (i) mean destructive field (MDF) around 20–30 mT (e.g., IC34-08A and TSS2-4B, Figure 3a) and (ii) MDF around 70 mT (e.g., ANE4-5A, Figure 3a). In spite of this difference, all samples are unidirectional, going to the origin, and with the same direction. On the other hand, their behavior under thermal demagnetization is indistinguishable.

Type B (Figure 3b) shows two clear components (*H* and *L*) in different proportions. In ANF5-2, component *L* is the carrier of 80% of the total magnetization (destroyed at 100–325°C and 4–40 mT) and component *H* of 20% (from 500 to 575°C). However, in ANE1-6 and ANE1-4, component *L* carries 30% (100–300°C) in Th demagnetization and 10% (0–12 mT) in AF, whereas *H* component carries 50% (500–585°C) or 70% in AF (from 35 to more than 100 mT) of the total magnetization. In AF demagnetization, these components show overlaps, being either possible (ANE1-4) or not (ANE2-9) to differentiate them. Intermediate terms between these two end-member behaviors can be observed (e.g., Th demagnetization of ANE2-9).

Finally, in Type C behavior, *H* component cannot be defined (Figure 3c). In some of these samples, *L* component is clearly present (ANF1-6; Figure 3c) and in others there exists a high-temperature component but with greater dispersion at site level (TRF3; Figure 3c), perhaps because of overlapping. Consequently, samples that show erratic behavior, overlapping components, major behavior differences in the same site and/or generating large error in the site means were not used for paleomagnetic interpretation.

L component was calculated in 7 out of the 33 sites, in Anergui, Anefgou, and Tirrhist massifs. This component shows minor dispersion, with a mean direction overlapping the expected directions between 20 Ma and the present day (Figure 4). The characteristic component, *H*, appears in 22 sites, with mean directions (Figure 4 and Table 1) showing a significant dispersion for each sample.

5.2. Magnetic Mineralogy

Temperature-dependent induced magnetization curves (Figure 5a) show a good correspondence with Types A and B coming from the NRM behavior. Rocks of Type A, with only *H* paleomagnetic component, show a magnetic phase with 580°C Curie temperature. Rocks of Type B, with *L* and *H* paleomagnetic components, show two magnetic phases; one of them is the 580°C temperature phase and the other presents lower Curie temperatures (330–580°C) (Figure 5a). This latter phase is not present in the cooling loop, indicating that it is destroyed during heating probably because of oxidation to hematite. Samples have low saturation fields (around 200–250 mT) in the IRM acquisition, higher in general when the low-temperature phase is more developed (Figure 5a).

Susceptibility temperature curves (Figure 5b) also evidence a drop of the magnetic susceptibility at 580°C and show the typical signature at −150°C related to the Verwey transition (Verwey, 1939; Walz, 2002). Homogeneous magnetic susceptibility in the heating loops between −100°C and 400°C evidences a minimum contribution of paramagnetic minerals to the total susceptibility since paramagnetic minerals show hyperbolic decreases with the increase of the temperature. This is in agreement with the similar bulk susceptibilities obtained at room and low temperature (−195°C, Figure 5c).

Day plot (Day et al., 1977; Dunlop, 2002) for different samples shows a mixing between single domain (SD) and multidomain (MD) magnetite (Figure 5d), independently of the NRM classification. The same experiment made for the whole rock and extracts of silicates of a hand sample of ANF2 site evidences the presence of magnetic minerals inside the silicate crystals, with magnetic properties similar to the whole rock, and clustered in the pseudo single domain (PSD) (Figure 5e).

Therefore, rock magnetic experiments show good correspondence with Types A and B coming from the NRM behavior. Rocks with low-temperature paleomagnetic component (*L*) show low to intermediate Curie temperature phase, which is absent for samples lacking the *L* component.

AGU Tectonics

10.1002/2017TC004578

Table 2
Scalar and In Situ Directional Data of the RT-AMS

		Magnetic scalar data										Magnetic directional data							
												k_{max}		Conf. angles		k_{min}		Conf. angles	
Site	*n*	*km*	*e*	*Pj*	*e*	*T*	*e*	*L*	*e*	*F*	*e*	Dec	Inc	Dec	Inc	Dec	Inc	Dec	Inc
ANE1	12	1.5	0.8	1.01	0.01	−0.050	0.424	1.006	0.005	1.007	0.008	264.1	19.1	41.8	6.7	125.4	65.2	53.4	8.1
ANE2	14	4.9	2.1	1.04	0.02	0.242	0.328	1.015	0.010	1.024	0.011	75.0	4.4	48.9	15.9	193.1	80.7	18.7	14.1
ANE3	14	6.4	1.4	1.08	0.03	0.598	0.272	1.015	0.013	1.058	0.023	98.9	0.1	40.7	6.1	189.3	68.7	9.7	6.6
ANE4	19	8.9	1.3	1.04	0.01	0.332	0.233	1.013	0.006	1.027	0.008	158.9	33.2	17.3	5.0	30.3	43.7	6.0	5.0
ANE5	19	19.9	6.0	1.02	0.01	−0.100	0.435	1.010	0.004	1.009	0.006	269.2	63.5	48.1	32.3	69.0	25.0	57.7	33.6
ANF1	14	15.2	11.1	1.02	0.01	−0.130	0.405	1.010	0.005	1.008	0.004	170.6	8.4	21.0	16.6	294.7	75.3	29.2	18.6
ANF2	9	11.8	9.5	1.10	0.03	0.362	0.255	1.030	0.018	1.061	0.021	0.6	43.6	61.7	11.9	207.0	43.2	15.4	11.9
ANF3	10	39.3	24.3	1.08	0.03	0.605	0.141	1.015	0.007	1.063	0.024	94.6	49.9	14.7	11.8	343.6	16.8	16.0	8.2
ANF4	10	13.5	2.5	1.17	0.10	0.391	0.311	1.039	0.015	1.121	0.087	269.1	64.0	13.4	6.0	172.3	3.3	12.9	4.8
ANF5	9	11.7	10.9	1.03	0.02	0.206	0.361	1.013	0.009	1.020	0.011	128.8	46.3	39.3	19.8	282.7	40.6	53.5	17.7
IC33	22	14.5	3.1	1.02	0.01	−0.130	0.405	1.012	0.005	1.009	0.005	57.3	26.4	14.2	8.0	217.6	62.2	42.3	8.5
IC34	18	10.4	1.0	1.02	0.00	0.133	0.268	1.007	0.002	1.010	0.003	359.1	0.9	12.1	6.6	267.2	63.4	10.7	7.1
IC35	6	15.7	15.5	1.12	0.09	0.670	0.107	1.018	0.017	1.090	0.062	95.0	23.1	66.1	16.6	351.5	28.7	31.6	9.7
IC36	18	12.3	2.6	1.02	0.01	0.067	0.327	1.008	0.004	1.009	0.004	263.8	21.5	20.9	14.0	356.0	5.5	23.9	12.5
TIR1	13	10.8	3.5	1.02	0.01	0.083	0.354	1.008	0.004	1.010	0.007	118.6	31.6	37.8	17.3	247.7	45.8	22.1	6.2
TIR2	7	96.2	37.7	1.02	0.01	0.244	0.548	1.007	0.005	1.014	0.009	178.9	8.8	70.3	38.4	293.8	69.8	39.3	25.5
TIR3	10	0.5	0.0	1.01	0.00	0.246	0.339	1.002	0.001	1.003	0.002	297.2	56.6	55.2	6.4	93.1	31.0	9.6	6.9
TIR4	9	11.8	2.3	1.02	0.00	0.000	0.517	1.008	0.004	1.009	0.005	11.1	8.8	35.3	31.1	176.9	80.9	46.8	21.7
TRF1	8	11.1	11.2	1.01	0.01	0.302	0.375	1.002	0.002	1.004	0.003	215.4	2.2	48.1	14.1	124.9	13.7	20.7	9.1
TRF2	13	76.5	15.2	1.12	0.03	0.341	0.138	1.036	0.013	1.074	0.016	152.2	12.7	36.0	11.1	38.3	60.8	19.4	6.4
TRF3	15	52.2	36.8	1.01	0.01	0.070	0.413	1.005	0.003	1.007	0.006	276.1	12.3	45.1	20.8	170.7	50.6	74.0	32.1
TRF4	13	103.0	36.2	1.03	0.01	0.006	0.489	1.015	0.008	1.017	0.012	124.3	24.2	22.8	17.2	312.6	65.6	34.1	16.4
TRF5	16	8.6	1.8	1.03	0.01	0.250	0.427	1.011	0.007	1.018	0.008	335.0	6.9	60.7	14.9	236.5	50.6	16.6	13.1
TRF6	17	3.5	2.5	1.10	0.04	0.552	0.274	1.018	0.009	1.074	0.034	172.9	40.7	52.0	7.7	293.3	30.5	16.2	6.6
TRF7	10	8.3	1.2	1.02	0.01	−0.160	0.541	1.012	0.005	1.010	0.007	1.8	55.6	54.2	21.9	172.4	34.0	49.9	27.1
TRF8	7	13.6	4.8	1.03	0.01	0.580	0.272	1.005	0.004	1.020	0.008	107.0	41.9	42.6	7.9	13.1	4.4	19.4	9.5
TSS1	13	9.8	8.6	1.08	0.04	0.399	0.347	1.020	0.016	1.052	0.027	160.6	25.2	33.2	11.6	293.4	55.3	17.3	11.5
TSS2	15	9.8	4.7	1.03	0.02	0.163	0.400	1.012	0.007	1.020	0.014	78.3	62.7	63.1	16.2	198.1	14.4	20.3	9.0
TSS3	7	21.0	14.0	1.02	0.01	−0.010	0.541	1.011	0.005	1.012	0.007	171.2	16.3	15.2	11.7	19.7	71.5	52.7	12.4
IC8	12	0.7	0.2	1.01	0.01	0.012	0.604	1.003	0.003	1.004	0.005	93.1	22.9	63.8	11.4	288.3	66.4	38.8	20.1
IC9	23	13.1	1.1	1.04	0.01	0.077	0.302	1.021	0.010	1.022	0.006	152.6	43.6	5.7	5.4	13.7	38.4	12.3	5.2
IC10	17	10.2	1.1	1.01	0.00	−0.030	0.372	1.005	0.002	1.005	0.002	9.6	18.6	40.3	9.9	273.1	18.7	23.7	10.0
IC30	15	9.3	1.3	1.01	0.00	0.038	0.369	1.006	0.003	1.006	0.002	47.1	67.9	33.0	11.0	286.3	11.8	29.4	14.0

Note. *n*: number of measured samples; *km*: bulk susceptibility; *Pj*: corrected anisotropy degree; *T*: shape parameter; *L*: magnetic lineation; *F*: magnetic foliation; *e*: standard deviation; conf. angles: confidence angle based on Jelinek statistics (Jelinek, 1981) calculated with Anisoft42 software (Chadima & Jelinek, 2009).

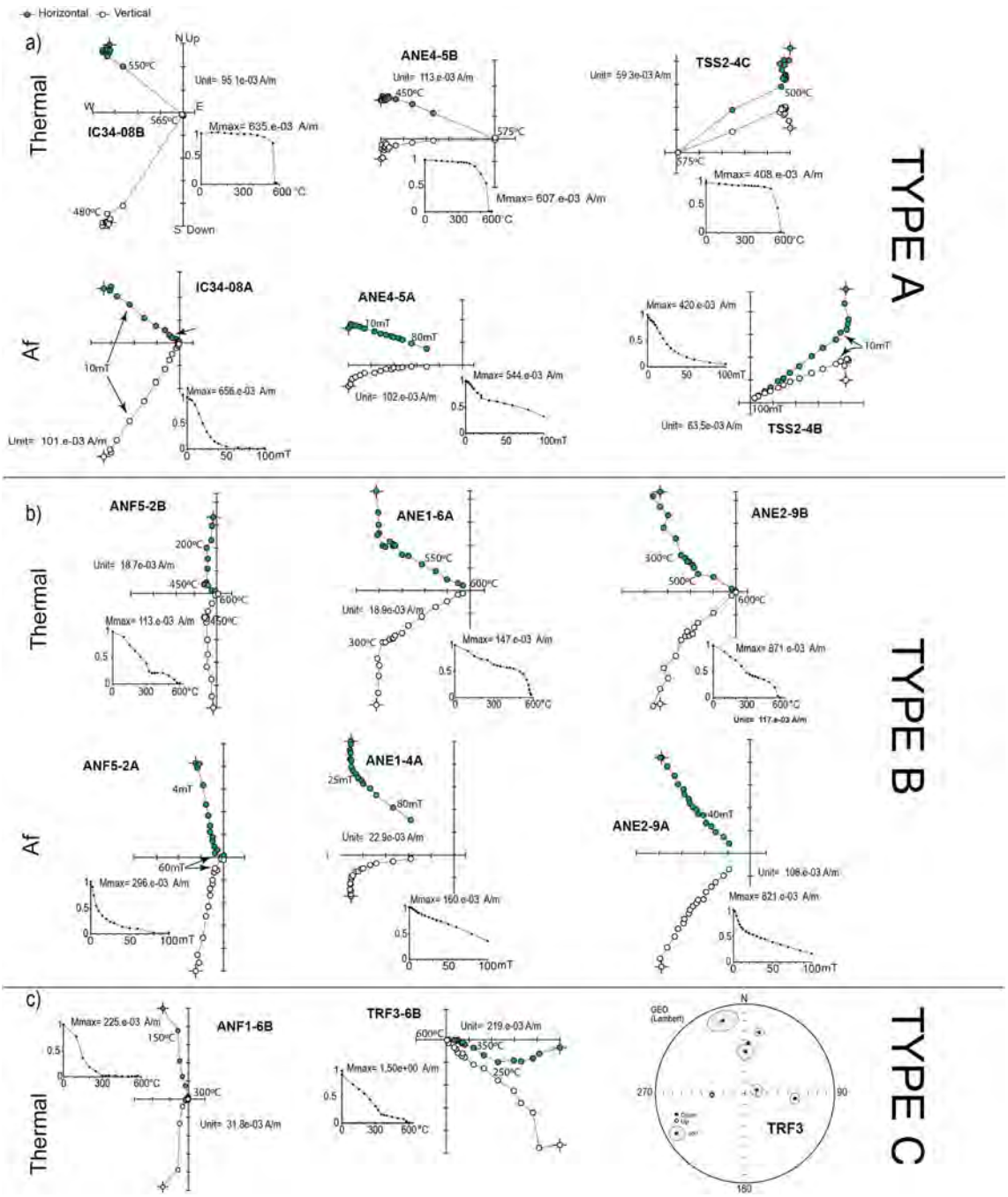

Figure 3. Orthogonal plots of NRM thermal and alternating field demagnetizations of representative samples, plotted in in situ coordinates. Filled symbols are projections onto the horizontal plane (north toward the up and east toward the right) and open symbols on the vertical east-west plane. Normalized NRM intensity is also shown. (a) Type A, characterized by unidirectional vectors that define the *H* component. (b) Type B, characterized by different development of *L* and *H* components. (c) Type C includes different behaviors with the common point of the absence of a reliable *H* component. ANF1-6 only presents the *L* component, and TRF3 shows a high-temperature component but with high dispersion at site level. Note that in Figures 2a and 2b, examples are shown in pairs of AF and Th demagnetizations, corresponding to two specimens from the same core.

5.3. Magnetic Fabrics

The gabbros show moderate to high magnetic susceptibility values, ranging between 0.3×10^{-3} and 165×10^{-3} SI. These values are distributed mainly from 1 to 20×10^{-3} SI, with more than 75% of the samples in this range and an average value of 18.54×10^{-3} SI (Table 2). These values are consistent with the presence of variable portions of magnetite, as indicated by the rock magnetic experiments. The mean ratio between

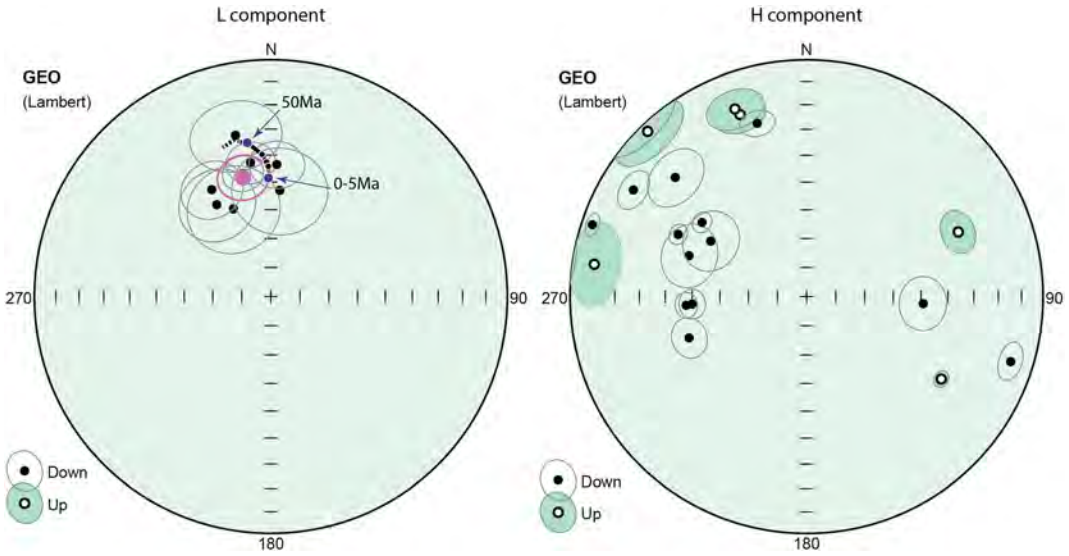

Figure 4. Equal-area projections showing the site mean directions of *L* and *H* components. Expected directions for NW of Africa between 50 and 0 Ma, obtained through the global apparent polar wander path (GAPWAP) (Torsvik et al., 2012), are also represented.

the bulk susceptibility at low and room temperature (Figure 5c) is 1.14, with values always very close to 1, indicative of the dominance of ferromagnetic minerals (s.l.).

Table 2 summarizes the scalar parameters for sites. Site means *Pj* values range from 1.002 to 1.407; high values of *Pj* dominate in Anefgou, western Tassent, and Tasraft (Figure 6). These values of *Pj* can be related to an igneous fabric (Tarling & Hrouda, 1993). Magnetic axes are well defined in most of the sites (Figure 6), regardless of the anisotropy degree. Overall, the magnetic foliation (*F*, plane whose pole is k_3) is better defined than the magnetic lineation (*L*, coinciding with k_1) and in most sites k_3 is well clustered and k_1 appears either well clustered or scattered, together with k_2 along a girdle defining the *F* plane. Maximum mean values of *F* and *L* factors are 1.121 and 1.039, and their mean values are 1.027 and 1.013, respectively. Few sites (e.g., IC33, Figure 6) show markedly prolate ellipsoids with clustered k_1 axes and a girdled distribution of k_2 and k_3. Although in each site the orientation of axes for different samples is consistent at the site scale, a noteworthy point is the strong difference in orientation between sites, even if located along the same structure.

In order to check the distribution of the RT-AMS axes and because of the possibility of finding intermediate and inverse magnetic fabric due to SD magnetite (Potter & Stephenson, 1988), RT-AMS has been compared with LT-AMS and AARM measurements. Most sites show normal geometry of the AMS because of the coincidence of the minimum axes of RT-AMS, LT-AMS, and AARM (Figure 6); maximum axes are not so well defined because fabrics are mainly oblate. However, some sites show intermediate fabrics. In IC10, LT-AMS and AARM are similar but different to RT-AMS (minimum and intermediate axes switching), indicating that the SD effect disappears at low temperature because of the enhancement of the paramagnetic signal; coincidence between RT and LT-AMS also agrees with magnetite and paramagnetic minerals carrying a similar magnetic fabric. IC34 shows similar distribution in RT-AMS and LT-AMS but different in AARM, indicating that both RT-AMS and LT-AMS are carried by SD magnetite. Finally, TIR1, TSS2, and TSS3 show slight deviations between the three magnetic fabrics. In summary, comparison between RT-AMS, LT-AMS, and AARM supports that RT-AMS generally shows normal magnetic fabrics carried by MD magnetite, but in some sites, both RT-AMS and LT-AMS reveal intermediate or inverse fabrics indicating a main contribution of SD magnetite to the magnetic fabric.

Furthermore, the significance of the magnetic fabric in relation to the petrofabric has been checked by comparison with 18 thin sections analyzed under the petrographic microscope. Thin sections (Figure 7) are perpendicular either to the observed foliation (when it was observable in hand samples or outcrops) or to the magnetic foliation. In general, the thin sections show a clear preferred orientation of tabular crystals of

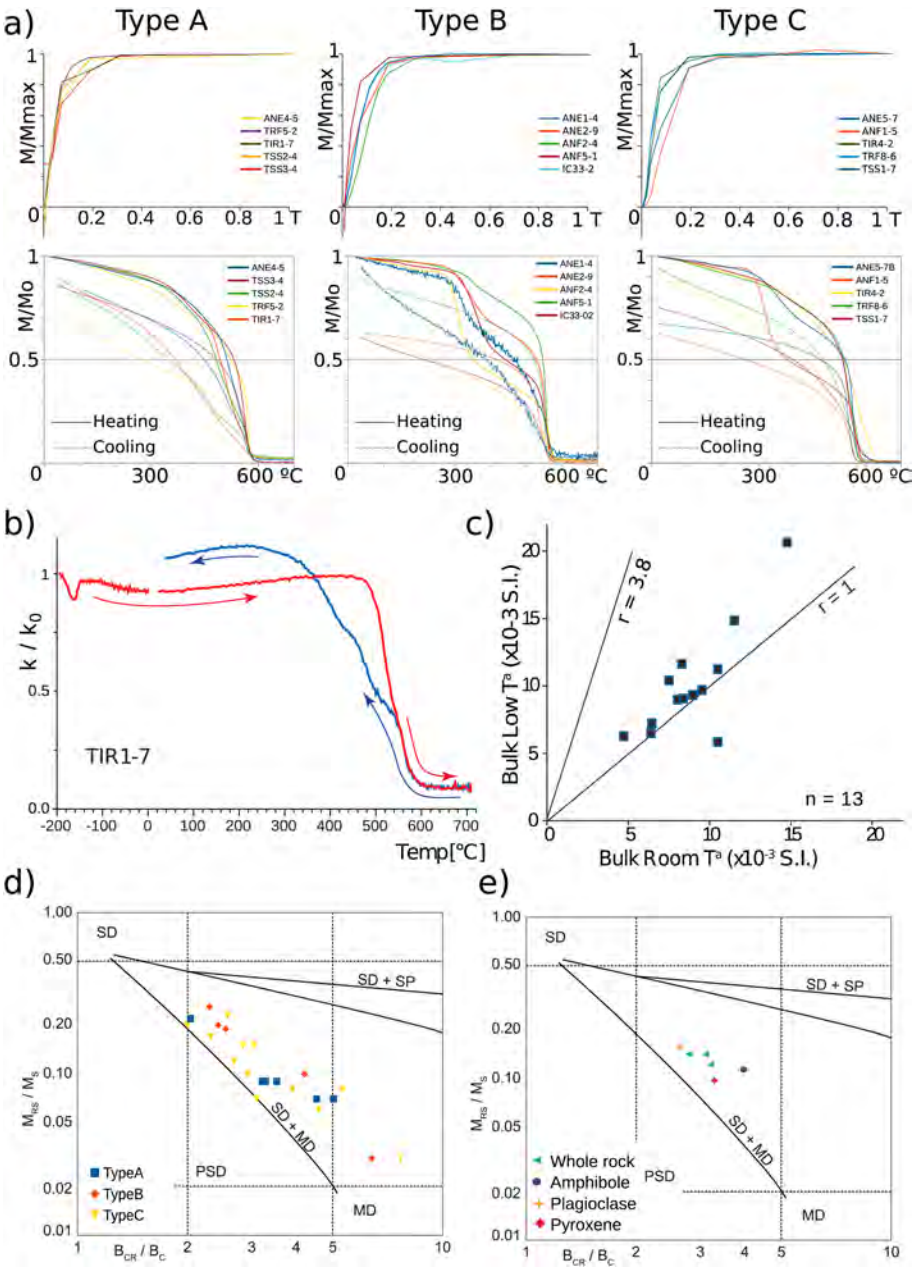

Figure 5. (a) Isothermal remanent magnetization (IRM) acquisition curves and temperature-dependent induced magnetization curves of the different behavior observed in the NRM analysis (Types A, B, and C). (b) Temperature-dependent susceptibility curve from liquid nitrogen temperatures corresponding to sample TIR1-7 (Type A in the NRM behavior). (c) Susceptibility at low (77 K) and room temperature (295 K) showing 1 and 3.8 ratios. (d) Day plot (Day et al., 1977) showing the hysteresis parameters for representative samples of different gabbro outcrops and (e) for the whole rock and extracts of silicates of sample ANF2-4. Classic areas of single domain (SD), pseudo single domain (PSD) and multidomain (MD) are plotted. Theoretical mixing curves (Dunlop, 2002) are also shown (SP, superparamagnetic).

plagioclase, coincident with the magnetic fabric (with deviations lower than 10°). In some sections, plagioclase crystals define two or more orientation maxima, but a dominant trend can be normally determined. The coincidence between large crystals orientation and the magnetic fabric agrees with models (Tarling & Hrouda, 1993; Usui et al., 2006, and references therein) stating that ferromagnetic minerals (s.l.) are usually aligned with large crystals whose orientation was acquired at high temperatures due to hydrodynamic forces during fluid or plastic magmatic flow. This has also been observed, for instance, by O'Driscoll et al. (2008) and Pueyo Anchuela et al. (2014).

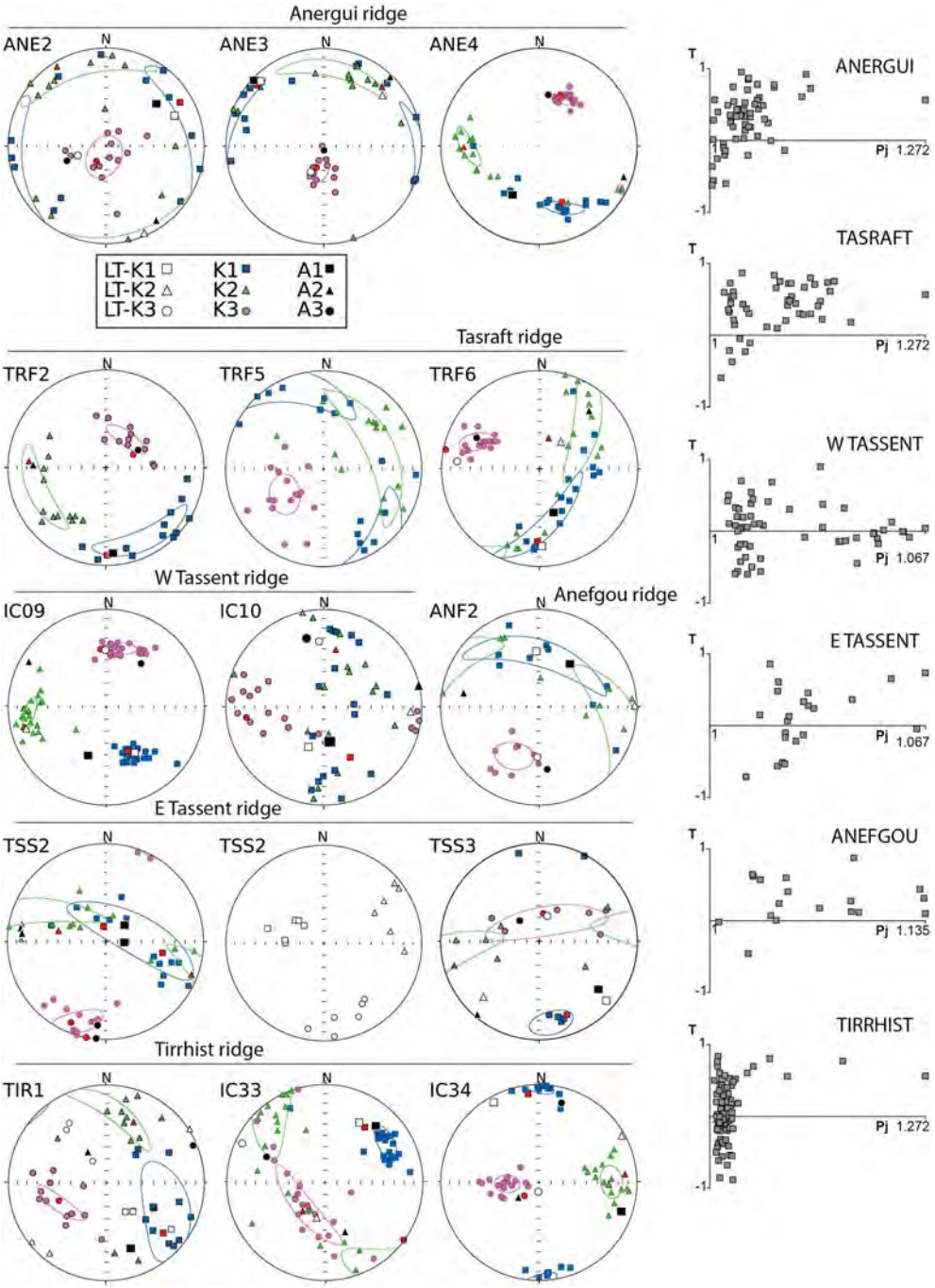

Figure 6. Equal-area projection of in situ magnetic fabrics (RT-AMS in colors, LT-AMS in white, and AARM in black) and *Pj-T* diagrams of the different gabbro massifs.

6. Interpretation of the Paleomagnetic Components

6.1. Magnetic Carriers

There exists a correlation between *L* and *H* paleomagnetic components, on one side and the magnetic phases with low and high Curie temperature observed in the thermomagnetic curves, on the other. The paleomagnetic direction of the *L* component is similar in the different sites and close to the present-day magnetic field (Figure 4), indicating that it is a secondary component generated after the Cenozoic compression

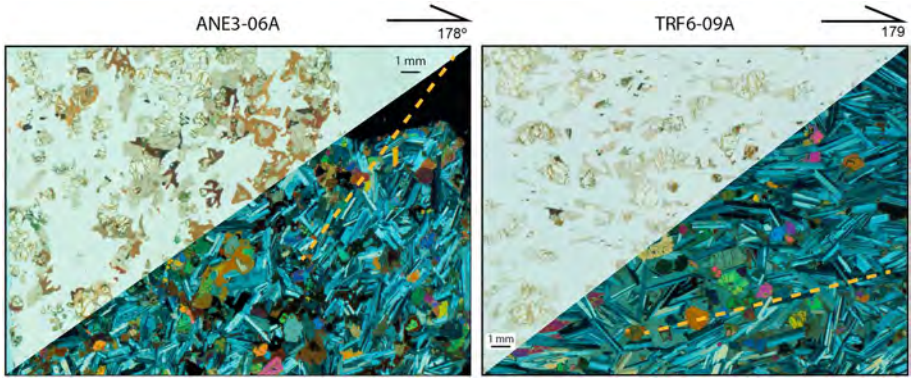

Figure 7. Microscopic images (parallel nicols at the top and crossed nicols at the bottom) of two selected samples. The thin section is perpendicular to the petrofabric foliation so the lineation defined by plagioclases in the thin section is the foliation of the rock. In orange, projection of the magnetic foliation onto the thin section plane.

(it does not record any rotation); this component could be related to alteration during the exhumation of the chain or with weathering. Curie temperatures of the low-temperature phase could be related to titanomagnetite; gradual variations of the Curie temperature between samples can be related to changes in Ti-Fe ratio and different degree of oxidation. Because of the slightly higher coercivity observed in the IRM acquisition curves, in the samples with this magnetic phase, changes on the Curie temperature could be rather related to different degree of oxidation.

Regarding the *H* component, NRM demagnetization diagrams (Figure 3) show a typical behavior of almost pure magnetite, coinciding with results from rock magnetic experiments (Figure 5). Noteworthy, this magnetite shows medium to high coercivity in AF experiments in some samples (e.g., ANE4 and ANE1; Figure 3). This behavior was observed in gabbros having inclusions of exsolved magnetite in silicate crystals (Ebert et al., 2010; Evans et al., 1968; Feinberg et al., 2005), and this is in agreement with rock magnetism experiments carried on silicate extracts (Figure 5d). However, the presence of additional fine-grained magnetite outside the silicate crystals cannot be discarded.

6.2. Origin of the *H* Component

Ensuring the primary character of a paleomagnetic component is a difficult matter in paleomagnetism. The lack of paleohorizontal reference on the gabbros, the high dispersion of the paleomagnetic mean directions, and the absence of baked contact tests makes this matter even more complex. In these points we analyze and justify the possible primary origin of *H* component:

1. The site mean directions of *H* component (Figure 4) show strong dispersion due to block rotations presumably during the Cenozoic inversion of the basin. Therefore, the *H* component was acquired before the Cenozoic.
2. There exists evidence about the presence of SD magnetite, such as inclusions in silicates that usually carry a very stable primary thermoremanence (Ebert et al., 2010; Evans et al., 1968; Feinberg et al., 2005).
3. Magnetic properties, that is, the medium to high coercivity (>100 mT) of a fraction of the *H* component, indicate a probable origin of the carrier (magnetite) related to high-temperature exsolution processes. These processes usually happen at temperatures above the Curie temperature of magnetite (Ebert et al., 2010).
4. Baked contact tests carried on Upper Jurassic-Lower Cretaceous dykes with carbonates as host rocks in the CHA (Villalaín, Casas-Sainz, & Soto, 2016; Villalaín, Ruiz, et al., 2016) show that dikes are not affected by the Cretaceous CRM observed in limestones. This agrees with results from other works that indicate that the primary component is preserved in gabbro bodies even after reheating due to younger intrusions (Denyszyn et al., 2013; Evans & McElhinny, 1966) or after metamorphism/metasomatism (Pariso et al., 1996).

Considering all these facts, and in light of previous works in similar materials, we can reasonably assume that the magnetite generated by high-temperature exsolution processes and/or appearing as inclusions within

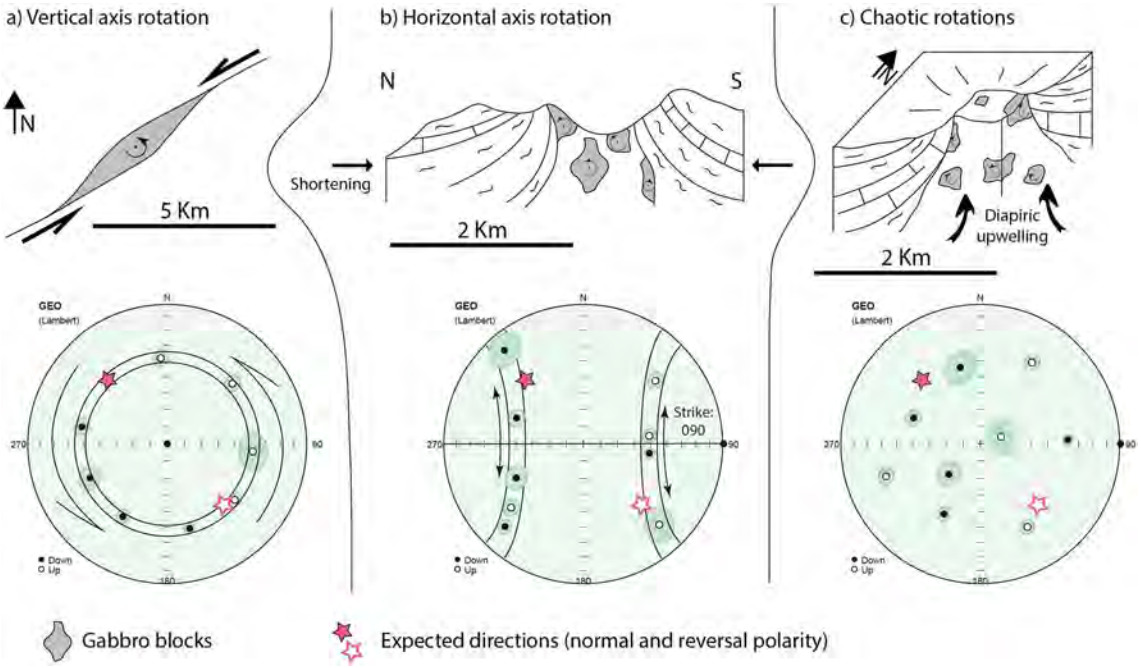

Figure 8. Equal-area projections showing hypothetical dispersion of paleomagnetic directions due to: (a) vertical axis rotations in a strike-slip context, (b) horizontal axis rotations for folding, or (c) chaotic rotations due to diapiric upwelling. In Figures 8a and 8b the small circles along which the paleomagnetic directions are expected are also shown.

silicate crystals is usually stable and carries a primary thermoremanence. Consequently, we consider *H* as a primary component. Since the target of this study is the deformation recorded by the gabbros as rigid bodies, a secondary magnetization acquired before the rotation stage would give similar information about this process.

Another major issue in paleomagnetic studies in igneous rocks is the averaging of paleosecular variation (PSV). Since the scatter of the 19 site mean directions of *H* component is notoriously high ($k = 5$), we cannot interpret it (exclusively) in terms of PSV, and therefore, tectonic rotations between sites must be involved. The corresponding virtual geomagnetic poles dispersion for the studied gabbros ($S_B = 32.2°$) duplicates values referred to Jurassic lavas from similar latitudes (S_B ~15°; Biggin et al., 2008). In addition, the geomagnetic angular scattering recorded in plutonic rocks should be lower (due to their slower cooling rates, even partially averaging PSV at the sample level) than in lavas, thus reinforcing a tectonic interpretation for the scattered site mean directions obtained in this study. Granitic plutonic bodies having radii of 1 km cool to the solidus temperature in 60,000 years, whereas a body with radius of 10 km needs more than 1 Myr. (Spera, 1980). The studied igneous bodies have radii ranging from 1 km in the western area to more than 2 km in the east. Theoretically, these cooling rates (even considering other kinds of rocks) would suffice for averaging the PSV, which is a matter of a few kiloannums. However, it is necessary to consider that the PSV can be a source of uncertainty in the quantitative interpretation of our results (~15° as maximum).

7. Analyzing the Paleomagnetic Directions in Gabbroic Rocks

Restoration of paleomagnetic vectors and AMS ellipsoids in igneous rocks is more complex than in sedimentary rocks due to the general lack of paleovertical or paleohorizontal markers. Some attempts have been done assuming that the dikes cutting across the gabbros were originally vertical: Hurst et al. (1992) restored the Troodos ophiolite using rotations of the paleomagnetic directions along small circles, constrained by the orientation of the dikes and the reference paleomagnetic direction.

According to this line of logic, the paths followed by paleomagnetic directions undergoing block rotations can be analyzed and compared with the dispersion observed in the paleomagnetic component *H*. This rotation processes are linked with three geological models that explain the tectonic evolution of the cores of

anticline ridges (Figure 8): (i) According to Laville and Piqué (1992), Jurassic igneous rocks were emplaced under a left lateral transpressional tectonic regime; if the *H* component were blocked before the end of these tectonic movements, the latter would generate a dispersion of the paleomagnetic component along a small circle with vertical axis (vertical axis rotation, Figure 8a). (ii) If the gabbros were rotated during, and consistently with, the Cenozoic folding of the anticlines, the dispersion should be in accord with a small circle with horizontal axis parallel to the tectonic structures (Figure 8b). (iii) Finally, if this dispersion is due to late diapiric upwelling without tectonic control, a chaotic dispersion of paleomagnetic directions is expected (Figure 8c). A chaotic dispersion could also result from the superposition of processes (i) and (ii) (horizontal and vertical axis rotations).

Although these models are oversimplified, their correlation with data can help to define the postemplacement history of these rocks, closely related to the tectonic evolution of the area. In the next subsection we analyze individually the paleomagnetic vectors obtained in each of the studied structures.

7.1. The Tirrhist-Anefgou Setting

The massifs of Tirrhist and Anefgou (Figure 9a) provide the key to elucidate the processes involved in the structuring of the gabbroic bodies and therefore in the scattering of the paleofield vector (*H* component). In equal-area projection (Figure 9b), these directions are scattered along a small circle with horizontal axis, whose trend is E-W. This small circle contains the expected paleomagnetic direction for this area during Jurassic times, obtained from the global apparent polar wander path (GAPWP) (Torsvik et al., 2012) in local coordinates. Therefore, variable clockwise (CW) rotations along this small circle and looking to N90°E are necessary to adjust the obtained paleomagnetic vectors to the Jurassic direction (except for IC33, which needs a minor counterclockwise, CCW, rotation, around 10°; this direction can be considered as indistinguishable from the expected direction and practically in situ). Therefore, the gabbros and their primary paleomagnetic directions have been affected by a CCW rotation after cooling (Table 1). The rotation around an E-W axis is consistent with the tectonic structures observed in the core of the anticline (E-W folds involving the limestones, Figure 9c, and minor thrust affecting both sedimentary and igneous rocks) and the CCW rotations agree with the NNW vergence of the Tirrhist anticline.

Following the works by Villalaín et al. (2003) and Villalaín, Casas-Sainz, and Soto (2016), the limbs of the Tirrhist anticline, where limestones affected by the circa 100 Ma remagnetization crop out, can be restored to the moment of the remagnetization acquisition. There, it is possible to obtain the paleodip of beds and to make a comparison between the deformational history of these limbs and the closest igneous rocks sites (IC33 and IC35). Paleomagnetic directions obtained from limestones at the limbs of the Tirrhist anticline (Figure 9d and Table 1) show that (i) its NW limb (CTR9) was affected by a strong CCW rotation (45° looking to the azimuth of the bed, N059°E) after the remagnetization stage, and (ii) its SE limb is affected by a smaller CCW rotation (about 17° looking to N081°E). After this procedure the NW limb showed a steep dip at circa 100 Ma (329, 79) (bedding as dip direction and dip) and the attitude of its SE limb was similar to its present-day position (171, 54) (Figure 9d). Therefore, the rotation axes and the amount of rotations are similar in limestones and gabbros (Figure 9d). However, note that IC35 shows a rotation axis slightly different from the closest limestone site (CTR9; see Figure 9d), thus indicating that there exists a small decoupling between the limbs and the core of the anticline.

7.2. Defining Criteria for Paleomagnetic Restoration

In the Tirrhist-Anefgou case, only one horizontal axis was used to restore the paleomagnetic directions (the simplest solution). However, there is more than one solution (i.e., axis trend) to restore the paleomagnetic vector to a feasible direction because two polarities, normal and reverse, are possible. In this way, there are two different solutions (horizontal axes and their corresponding small circles) to restore paleomagnetic directions. Note that the emplacement age of the gabbros circa 150 Ma is characterized by a high reversal rate of magnetic polarity (Gradstein et al., 2012) and both solutions could be right. These two axes have necessarily different direction, and the one having a better match with the geological features (trend of the main and minor structures at the core of the anticlines) was chosen. Moreover, AMS axes can be restored in the same way that the paleomagnetic directions (considering that blocking of the characteristic paleomagnetic component and the magnetic fabric acquisition is geologically coeval). Therefore, coherence between

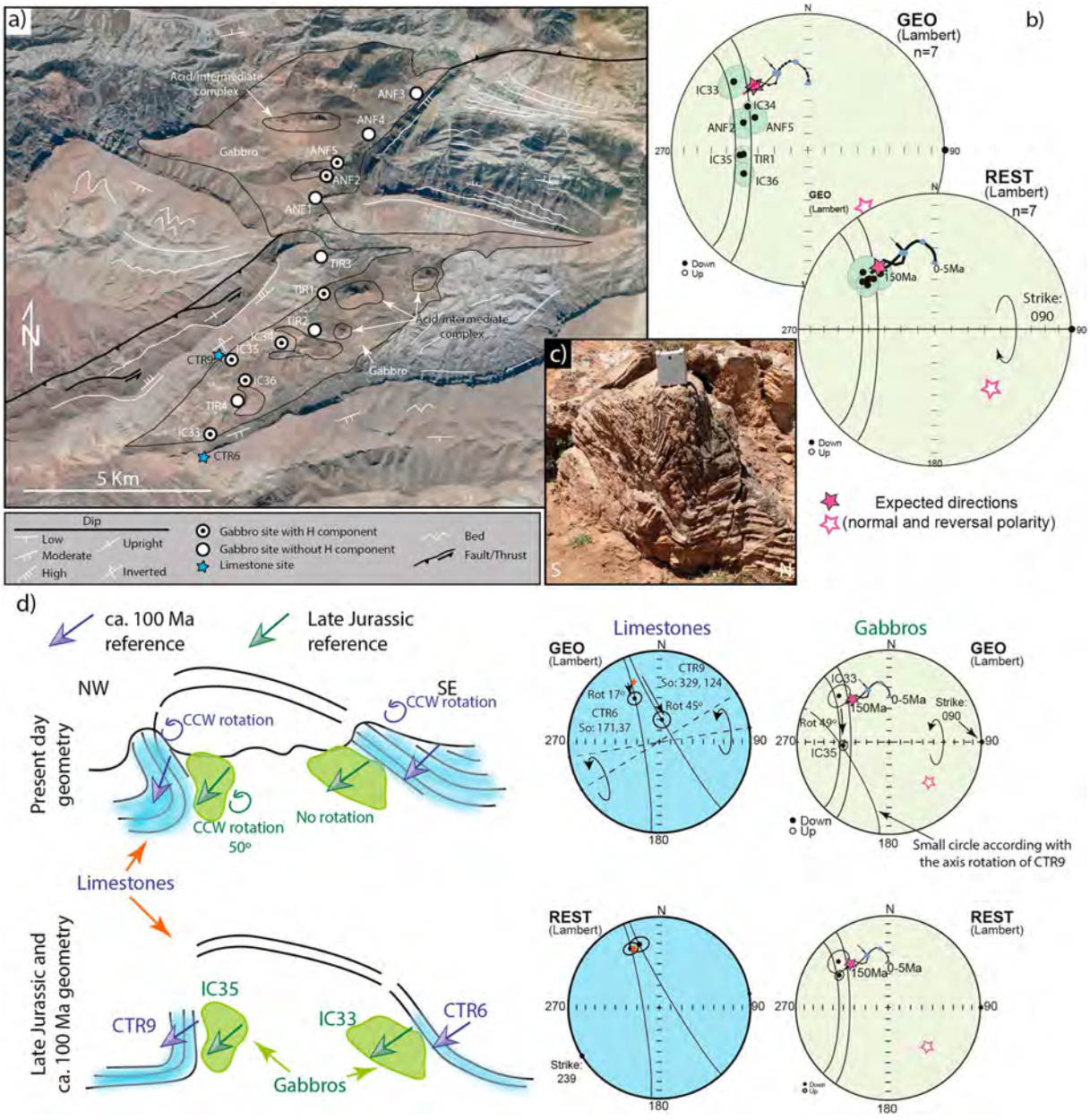

Figure 9. (a) Google Earth image of the Tirrhist-Anefgou massif with the location of the paleomagnetic sites and some geological features. (b) Equal-area projections showing the mean directions for the characteristic magnetization (*H* component) and 95% confidence circle obtained in Tirrhist and Anefgou gabbros, before (GEO coordinates) and after (REST (Restored) coordinates) the rotation correction toward the Middle-Late Jurassic reference. The seven paleomagnetic directions show dispersion along a small circle with E-W horizontal axis. Mesozoic-Cenozoic expected directions for NW of Africa obtained through the global apparent polar wander path (GAPWAP) (Torsvik et al., 2012) are also represented. Violet star shows the expected direction for the gabbros cooling age. (c) E-W syncline affecting a Triassic-Jurassic limestone site in the core of the Tirrhist anticline. (d) Current geometry of south and NW limbs of the Tirrhist anticline (CTR6 and CTR9 sites) and the closest gabbro sites (IC33 and IC35, respectively) and reconstruction to the paleogeometry at the time of the magnetization acquisition (note that this time is different for the gabbros and for the limestones). Equal-area projections showing mean paleomagnetic directions for CTR6, CTR9, IC33, and IC35, in in situ coordinates (GEO) and after restoration to the expected direction of the remagnetization (REST). The optimal directions, close to circa 100 Ma and circa 150 Ma directions for limestones and gabbros, respectively, and the disposition of the limb for this age are also represented.

AMS data from the different sites for each structure was also checked according to the two different rotation routines for normal and inverse polarities

Finally, once the axis of rotation has been chosen, it is possible to perform the restoration in CW or CCW sense, for 360° as sum of the two angles. When the two angles were very different, the smaller angle

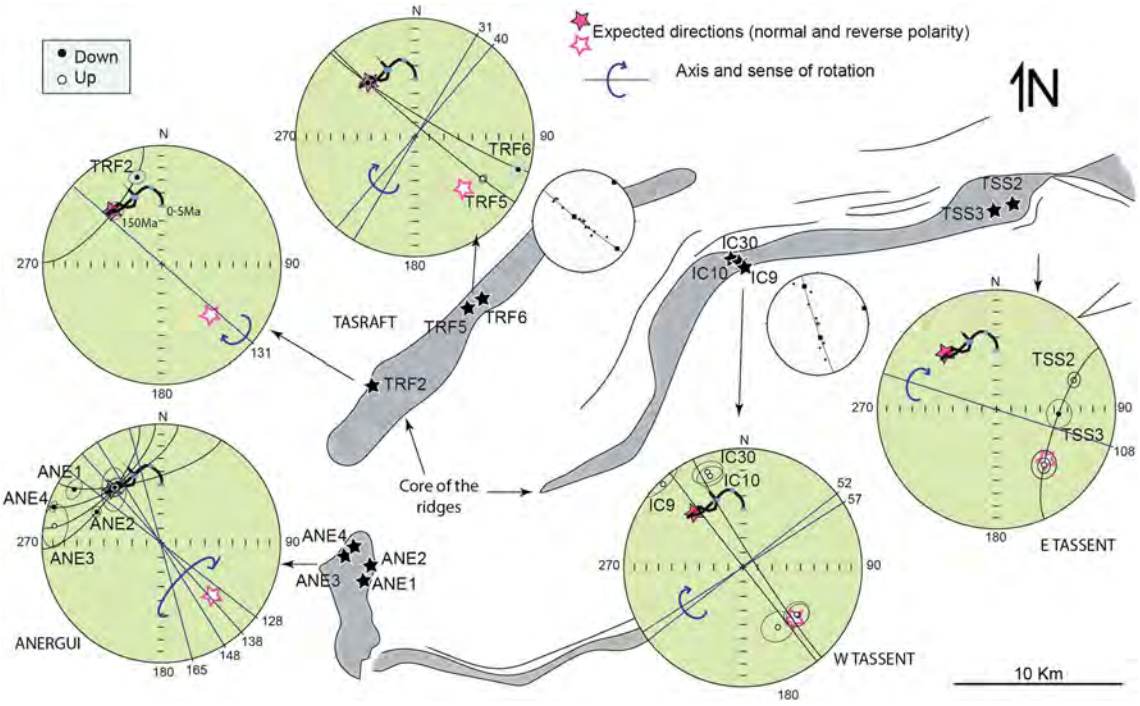

Figure 10. Paleomagnetic restoration of Anergui, Tasraft, and Tassent sites. The mean site directions of the *H* component are represented in equal-area projections. Each diagram shows the in situ paleomagnetic direction of the different sites and the restored direction to the Jurassic position (see Figure 9). Each diagram has the corresponding small circle, which joins the in situ with the Jurassic paleomagnetic directions as well as the orientation of the axes of rotation underwent by the bodies. Available bedding data and their cylindrical best fit are also represented in equal-area projection (white stereoplots).

was chosen. However, there is a higher uncertainty when both solutions are similar (amount of rotation close to 180°).

Hence, although there can be different paths to restore paleomagnetic vectors, throughout this process we have chosen the simplest (only one axis of rotation following the smaller rotation) and geologically more reasonable (structural trends and minimum rotation angles) path to restore the paleomagnetic directions.

On the other hand, it is important to remark that the goal of this work is to analyze the deformational patterns of the core of ridges instead of a detailed reconstruction of the rotational history of the gabbros (perhaps an impossible task at this time). This is the reason that we use some simplifications that allow us to define some common patterns. As an example, uncertainties linked to mean paleomagnetic directions (i.e., α_{95}) have not been quantitatively considered because they do not contribute to obtain more accurate results and are another error source, increasing the complexity of the problem. All in all, this restoration method was used to obtain qualitative but not quantitative (i.e., paleopoles) results and restored paleomagnetic directions of the ridges were obtained (Figure 10 and Table 1), as we describe in the following subsections.

7.3. Paleomagnetic Restoration

In the Tassent ridge, the *H* component was clearly isolated in five out of seven sites (two in the eastern sector and three in the western one). The directions from the two sites of the eastern sector (TSS2 and TSS3) lie in a small circle (with ESE axis), which also includes the expected reverse polarity direction for Jurassic times at the study area. Rotations necessary to restore the calculated paleomagnetic directions to this Jurassic direction are high but consistent with the main structural trend and local folds. Nevertheless, the western sites need a NE rotation axis, different from the eastern sector but consistent with the main trend of the ridge (bedding data agree with the rotation axis). In comparison with the Anefgou-Tirrhist massif, Tassent gabbros record important rotations. In both eastern and western areas, the sense of rotations registered in the gabbros (finite rotation since their emplacement until present) is CCW looking to the east.

Only in three out of the eight sites of the Tasraft ridge the *H* component has been isolated (Figure 10). Taking into account the same magnetic polarity for all sites, two restoring options are available.

1. Considering a normal polarity for the paleomagnetic direction (Figure 10), TRF5 and TRF6 show dispersion along a NE-SW small circle and TRF2 along a NW-SE one. The NE-SW axis (for TRF5 and TRF6 sites), but not the NW-SE axis necessary in TRF2, is consistent with the main trend of Tasraft antiform.
2. Considering the reverse magnetic polarity, TRF5 and TRF6 paleomagnetic directions and the reverse polarity direction for the Jurassic lie within a small circle with NW-SE axis. On the other hand, TRF2 needs a strong rotation along a NE-SW axis, parallel to the structural trend. Either of the two options implies two perpendicular rotations. Finally, Anergui paleomagnetic directions show CW moderate rotations along axes with NW-SE to NNW-SSE directions.

7.4. Interpretation of the Paleomagnetic Restoration

From the obtained results, paleomagnetic directions obtained from *H* component show an important dispersion that can be explained by horizontal axis rotations of the gabbro bodies. In Tassent, Tasraft, Anefgou, and Tirrhist (independently of the restoring option chosen for Tasraft), paleomagnetic directions record CCW rotations (looking to the NE-E) around axes parallel to the structures (E-W to NE-SW). This agrees with a tectonic control of rotation consistent with reverse, top-to-the-N-NW shear, in relation with overthrusting. However, diapiric processes can also be involved in the rotation of the gabbro bodies (mainly in Tasraft, where there is a high proportion of plastic rocks) generating rotations around other axes. Differences between rotation axes according to variations in the structural trend agree with a main control from the inherited extensional structures.

Tasraft and Tassent show stronger rotations of the gabbro bodies than Anefgou and Tirrhist ridges. This can be related to differential proportion between igneous and Triassic sedimentary rocks (mainly shales) at the core of the ridges. In Anefgou and Tirrhist, igneous rocks dominate with minor presence of shales; conversely, Tasraft and Tassent show important amount of shales in their cores. Dominance of sedimentary rocks (shales and evaporites) versus igneous rocks can allow stronger rotations of gabbro bodies or even differential rotations between close sites (e.g., TSS2 and TSS3).

The Anergui ridge shows a different pattern. In this case, block tilting driven by halokinetic processes is probably the cause for the dispersion in the paleomagnetic directions.

Finally, further discussion is necessary regarding the Tasraft ridge and the two proposed restoration options. There is evidence to support the option shown in Figure 10. First, the restoration of the AMS agrees better with this option. Besides, there is a differential rotation between TRF5 and TRF6 (Figure 10), in spite of being close sites; this could be more easily explainable by rotations related to tectonic processes (with rotation axis parallel to the structural trend) rather than only by a strong rotation of TRF6 (TRF5 would not record any rotation since it approaches the reverse polarity direction) due to diapiric processes (around an axis perpendicular to the structural trend). However, this does not have implications in the interpretations since the same rotation axes are necessary in both options. Nevertheless, it is true that the proximity of TRF2 and TRF5 paleomagnetic directions to normal and reverse polarity references, respectively (Figure 10), could indicate a different scenario in which the igneous rocks of this ridge could show different polarities.

In summary, restoration of the paleomagnetic directions indicates that tectonic structures imposed a major control on the rotation of gabbro units. Rotation axes are grouped into two main sets, NE-SW and E-W, coincident with the structural trend in each sector. This is indicative of the control of inherited geometry on the trend of the Cenozoic structures, generated under a NNW-SSE shortening (Ait-Brahim et al., 2002; Mattauer et al., 1977). Major rotations are observed in the structures with higher proportion of Triassic shales and smaller gabbro blocks (massifs of Tassent and Tasraft). This also clearly indicates the decoupling between the core and the limbs of the ridges since the limbs did not register rotations higher than 70° after remagnetization (Torres-López et al., 2016) and 90–100° in total. However, in the anticlines whose core is mainly composed by igneous rocks (Tirrhist and Anefgou), the rotations of the gabbro units are more limited and on the same order than recorded by the limestones. In either case, CCW sense of rotation in most sites can indicate reverse shear toward the north or NW, not readily apparent due to the strong symmetry of the Mesozoic structures (salt walls). On the other hand, moderate rotations in the southwesternmost sites (Anergui and south of Tasraft) may be related to block tilting associated with diapiric processes.

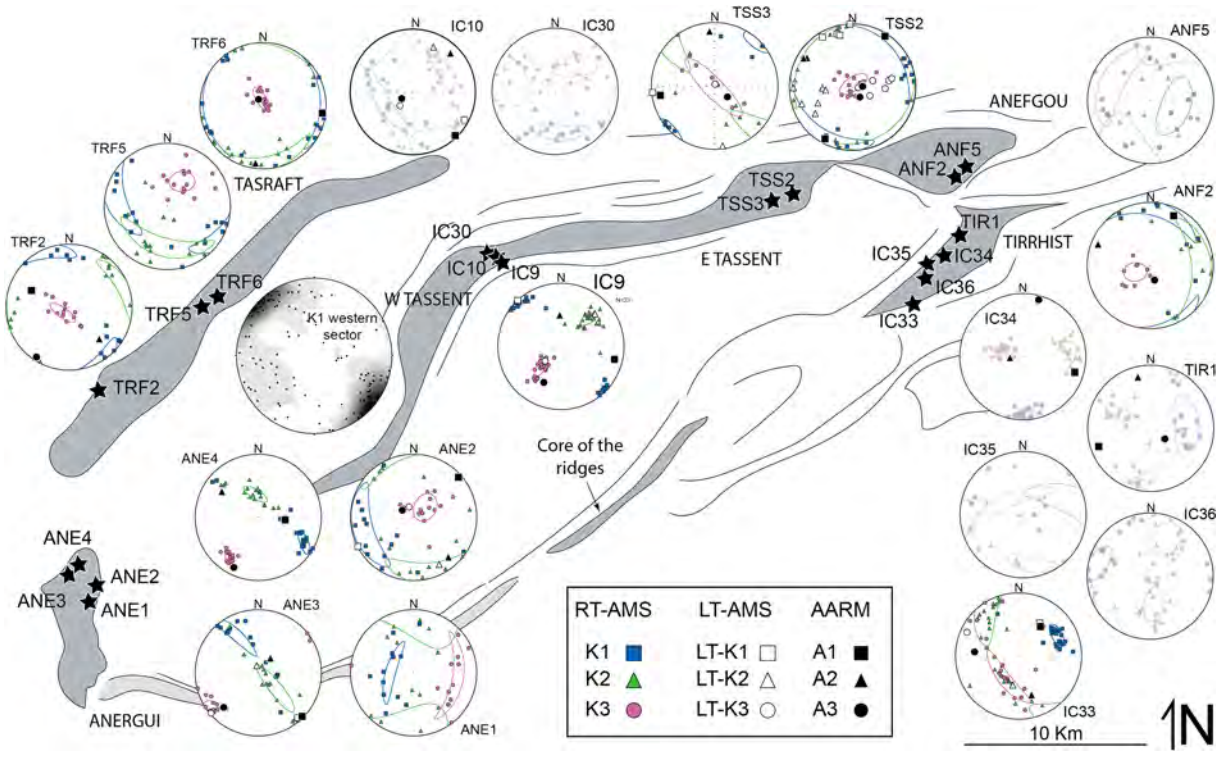

Figure 11. Equal-area projection of restored magnetic fabrics (RT-AMS, LT-AMS, and AARM). Only the sites in which paleomagnetic restoration is available are represented. Sites without confidence on normal carrier fabrics are represented with transparency. Contour plot of k_1 is represented for the western sector.

8. AMS Results and an Emplacement Model for the Gabbros

The gabbro bodies are characterized by brittle deformation; these processes did not modify the original magnetic fabric, since no indication for solid-state deformation was detected under the microscope (Figure 7), where texture and mineral arrangement are clearly primary generated during the solidification of the magma. Low *Pj* values of the AMS also are in agreement with a primary petrofabric rather than with solid-state deformation.

Gabbro bodies only crop out in the core of the ridges because of the presence of Triassic shales and evaporites, whose ductile behavior favored their emplacement; this unit is the main décollement, several hundreds of meters thick (Calvín et al., 2017; Saura et al., 2014), located at the bottom of the Jurassic carbonate sequence. When the magma reaches the ductile level during its ascent, expansion and replacing of the ductile level occurs, forming laccolith-shaped bodies, as shown in analogue models of sand-silicone systems (Román-Berdiel, 1999; Roman-Berdiel et al., 1995, 1997). The magnetic fabric acquired during magma solidification, blocked around 800°C when the plastic flow ceases (Tarling & Hrouda, 1993), can respond to (i) external tectonic control, determining the strain field in the region during magma emplacement and the kinematic framework controlled by its structural setting (Antolín-Tomás et al., 2009; Aranguren et al., 2003; Bouchez & Gleizes, 1995; Bouchez et al., 1990; Izquierdo-Llavall et al., 2012; Liodas et al., 2013; Román-Berdiel et al., 2006) and (ii) internal flow mechanisms not directly related to the strain conditions but rather to the behavior of magma within the magmatic chamber (Archanjo et al., 2012; Ferré et al., 2002; Maes et al., 2007).

Axes and angles of rotations obtained from paleomagnetic restoration can be used to restore the magnetic fabric directional data to the prerotation stage (Table 1). With the exception of ANE1 and ANE2, all sites from the western sector (Anergui, Tasraft, and western Tassent) show consistent directions after restoration (Figure 11). Magnetic lineation is subhorizontal with a main NW-SE direction independently on the trend of the ridge (e.g., compare IC09 and TRF sites). The magnetic foliation is subhorizontal in Tasraft and show

steep dips, with a NW-SE trend, in ANE-3 and ANE-4. Intermediate dips appear in other sites. Note that IC10 has intermediate RT-AMS (and probably also IC30 that shows similar RT-AMS properties), but AARM and LT-AMS follow the general trend for this sector.

Magnetic fabrics in the eastern sector (eastern Tassent, Anefgou, and Tirrhist) show a strong heterogeneity. Eastern Tassent sites show horizontal foliation and lineation; however, lineations show a high variability in trend. TSS2 shows both ENE-WSW and N-S trending lineations, but all prolate samples (negative *T* parameter) have ENE-WSW lineation, in agreement with the NE-SW lineation observed in TSS3. Horizontal foliation also dominates in Anefgou and Tirrhist, but the lineation is not well defined and only a weak pattern of E-W to N-S trend can be observed. Note that several samples of this area (those with transparency in Figure 11) show intermediate fabrics in AMS.

There are nearby sites (ANE3 and ANE4; TRF and TSS sites; Figure 11) that show a better clustering, even after applying the corresponding different rotations for each site. This is a complementary test supporting the correct restoration of the paleomagnetic and AMS data and also of the relative chronology of AMS and the blocking of magnetic fabric (i.e., magma solidification) that must predate solid-state rotation of igneous bodies. However, Tirrhist and Anefgou sites, where the paleomagnetic restoration is well constrained, show very different patterns and directions of their magnetic fabrics (Figure 11). This can be related to the internal conditioning of magmatic systems, such as differential magma fluxes.

In summary, western sites (western Tassent, Tasraft, and Anergui) are characterized by a NW-SE magnetic lineation. In both Tasraft and western Tassent ridges, the gabbro bodies are small and embedded within Triassic ductile rocks. In these cases, the magma was free to expand during its ascent and emplacement because the Triassic salts and shales acted as an isotropic medium. However, the pervasive NW-SE magnetic lineation indicates a preferred flow direction that can be related to the regional trend of extension; a NW-SE extensional stress favoring a magma expansion (and therefore a main flow direction) roughly parallel with it. This is consistent with the NW-SE to NNW-SSE extensional regime proposed for the Jurassic in this sector (Ait-Brahim et al., 2002). Magnetic foliation could be related either to lithostratigraphic pressure of the overburden or to ballooning during expansion of the intrusion.

The eastern bodies show a more heterogeneous magnetic fabric. This can be a response to the lack of available space for the intrusion. During magma ascent, the cooling magma would not be free to move laterally, thus conditioning the petrofabric. The roughly E-W to N-S lineation could be related to the shape of the bodies, which in turn were controlled by the geometry of the ridge and the fault system channeling magma upward to the emplacement levels.

9. Evolutionary Models of the Gabbros

Attending to the volume portion of gabbros in the core of the ridges and the subsequent behavior of the gabbro bodies during the evolution of the ridges, two kinds of structures can be distinguished (Figure 12). Tasraft type is characterized by small Jurassic igneous bodies embedded in a large amount of Triassic rocks, registering high rotations and the core is totally decoupled from the limbs; in Tirrhist type the core of the ridge is occupied mainly by Jurassic igneous rocks, and rotations are lower and similar for limbs and core (although a weak decoupling can also be interpreted). The ridges of the CHA and the rotations of the gabbro bodies are the result of three main stages (Figure 12):

1. Tilting of the bedding due to an early diapiric stage (Early-Middle Jurassic, Saura et al., 2014), mainly generating salt walls along inherited basement faults during basin formation, linked to extensional tectonics (Figure 12a).
2. Emplacement of igneous rocks during the Middle-Late Jurassic, partially using the gaps generated by the earlier diapiric processes, replacing the Triassic evaporites, and generating new structures of the host rocks, mainly in Anefgou and Tirrhist ridges. Diapiric processes were probably reactivated due to the activity of hydrothermal fluids that circulated along the ridges (Figure 12b) (Schofield et al., 2014). According to AMS, main flow direction in the Tasraft type is NW-SE, probably conditioned by the main NW-SE extensional tectonic regime, whereas in the Tirrhist type the main flow direction is roughly NE-SW, parallel to the main faults.
3. Basin inversion during Cenozoic shortening (Figure 12c) triggered an important erosion of Mesozoic sediments and exhumation of gabbros. Diapiric processes (Michard et al., 2011) affected the core of

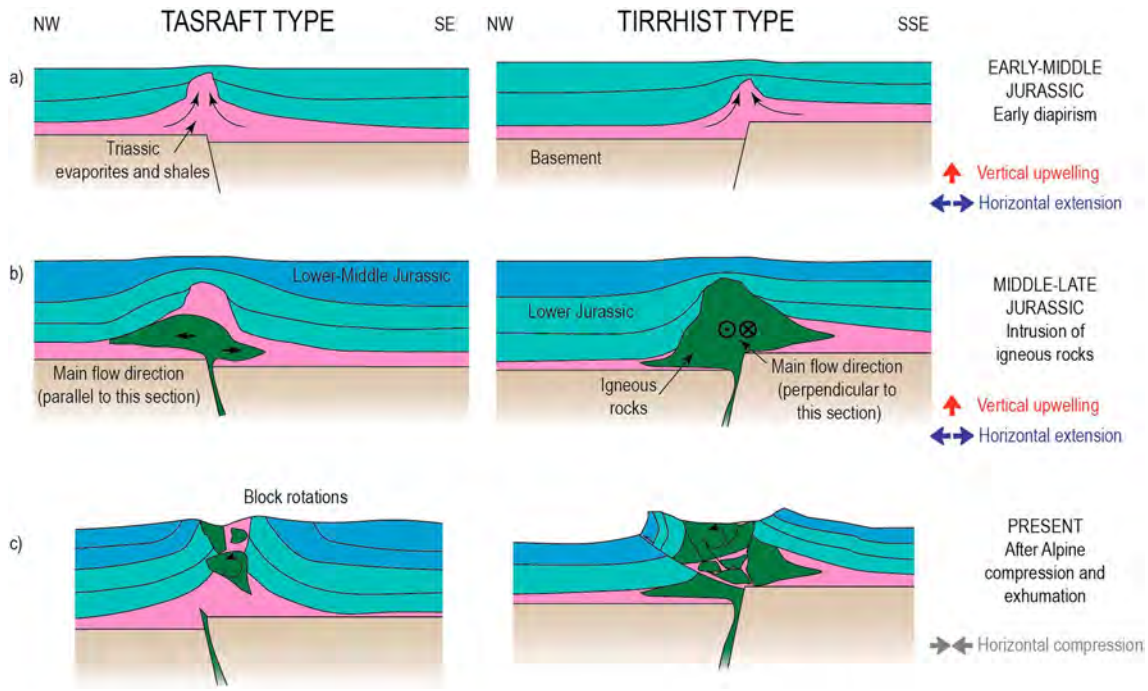

Figure 12. Evolutionary model of the two main kinds of structures found in the studied area, showing the main processes generating the ridges: (a) early diapirism predating the igneous intrusion, (b) igneous intrusion with deformation and reactivation of the diapiric processes due to the activity of hydrothermal fluids, and (c) Cenozoic shortening, exhumation and late diapirism (the latter intervening mainly in the Tasraft structure).

the ridges, especially in Tasraft and Tassent, where paleomagnetic analysis indicates strong rotations probably linked to a higher proportion of Triassic shales. However, according with the rotation pattern, these diapiric processes were conditioned by the trend of the structures and by the compressive tectonic regime, because rotations follow a systematic pattern and the scatter recorded by the paleomagnetic *H* component cannot be considered as random. Therefore, the Cenozoic rotation of the gabbros is interpreted as a consequence of compression and north verging thrusting instead of late diapiric processes.

Considering everything, two kinds of structures can be distinguished. On one hand, Anefgou and Tirrhist (Figure 12) are short structures with large amounts of igneous rocks in their cores and practically absence of Triassic shales. These structures are actually similar to eastern Tassent gabbro. Both the Tirrhist and Anefgou gabbros show minor to moderate horizontal axes rotations; gabbros close to the host rocks recorded similar Cenozoic rotations. This can suggest that these gabbros were emplaced in contact with the limestones, generating tilting of beds. However, absence of rocks younger than the Lower Liassic as roof pendants embedded in the igneous rocks (Armando, 1999) in Tirrhist-Anefgou massifs indicates that the gabbros were emplaced below the Lower Liassic limestones and that during the Cenozoic shortening they were uplifted (about 3–4 km in the Tirrhist-Anefgou massifs) undergoing only minor block rotations.

On the other hand, the gabbros of Tassent and Tasraft (Figure 12) show significant rotations related to abundant shales and consequently more freedom of movement within them. Finally, Anergui structure cannot be interpreted as a true ridge but as a significant accumulation of igneous rocks whose ascent was favored by fractures at the intersection between the Tassent and Ikkou ridges.

10. Conclusions

The paleomagnetic study in the central High Atlas gabbros allows to isolate the characteristic component in 19 paleomagnetic sites. This is interpreted as a primary thermal magnetization (i.e., a thermal remanence acquired by these igneous rocks during their cooling ages) carried by SD to PSD magnetite. At least part of this magnetite is forming inclusions in silicate crystals (pyroxene, amphibole, and plagioclase).

Distribution analysis of the paleomagnetic directions allows inferring horizontal axes rotations of the gabbro bodies in the Tirrhist-Anefgou massif and extrapolating this deformational model to other studied massifs. Two kinds of structures were differentiated according to both the rotation pattern (amount of rotation and orientation of rotation axis) and the outcrop pattern of each ridge. (i) Tirrhist type is characterized by wide, dome-shaped structures, with a large amount of Jurassic igneous rocks in their cores; small rotations ($<50°$) are registered, similar and coherent with the ones obtained in host rocks. (ii) Tasraft type is characterized by long structures with relatively small Jurassic igneous bodies embedded in a matrix of Triassic rocks.

Horizontal rotation axes used for restoration are E-W to NE-SW, parallel to each structure and indicating a tectonic control on the rotations. Strong rotations ($>90°$ in some sites) are recorded, much bigger than the ones registered by the host rock, indicating a decoupling between core and limbs due to the Cenozoic inversion. All sites record counterclockwise rotations (looking to the east and to the NE), indicating that they can be related to NW to north verging thrusting.

This study shows that this methodological approach can be a useful tool to restore igneous bodies lacking position markers.

Results from paleomagnetic analysis were used to restore the magnetic fabric to its prerotational stage. Magnetic fabric analysis (RT-AMS, LT-AMS, and AARM) combined with petrofabric studies infers normal fabrics in most of the sites, although in several cases intermediate to inverse fabrics (mainly in the eastern sector) occur. AMS is carried by magnetite that mimics the distribution of plagioclase crystals. Magnetic fabrics on the western sector show a prevailing NW-SE horizontal lineation that can be related to tectonic extension during the emplacement of igneous rocks. The eastern sector shows a more heterogeneous distribution in orientations, the direction of the prevailing lineations trending NE-SW, parallel to the main faults.

Acknowledgments

This study was financed by the research projects CGL2012-38481 and CGL2016-77560 of the MINECO (Spanish Ministry of Economy and Competitiveness) with also FEDER funding (European Union). P. C. also acknowledges the MINECO for the F.P.I. research grant BES-2013-062988. The authors acknowledge Abdelkader Mahmoudi and Hmidou El Ouardi for helping in field work and Carlos Rossi for carrying out the extracts of the silicate crystals. Institute for Rock Magnetism (University of Minnesota, USA) and specifically Mike Jackson are thanked for rock magnetic measurement support. The authors also acknowledge the constructive revisions, comments, and suggestion from Helga de Wall and three anonymous reviewers. Raw data are in the supporting information.

References

Ait-Brahim, L., Chotin, P., Hinaj, S., Abdelouafi, A., El Adraoui, A., Nakcha, C., … Chaouni, A. (2002). Paleostress evolution in the Moroccan African margin from Triassic to present. *Tectonophysics*, *357*(1-4), 187–205. https://doi.org/10.1016/S0040-1951(02)00368-2

Antolín-Tomás, B., Román-Berdiel, T., Casas-Sainz, A., Gil-Peña, I., Oliva, B., & Soto, R. (2009). Structural and magnetic fabric study of the Marimanha granite (axial zone of the Pyrenees). *International Journal of Earth Sciences*, *98*(2), 427–441. https://doi.org/10.1007/s00531-007-0248-1

Aranguren, A., Cuevas, J., Tubía, J. M., Román-Berdiel, T., Casas-Sainz, A., & Casas-Ponsati, A. (2003). Granite laccolith emplacement in the Iberian arc: AMS and gravity study of the La Tojiza pluton (NW Spain). *Journal of the Geological Society*, *160*(3), 435–445. https://doi.org/10.1144/0016-764902-079

Archanjo, C. J., Campanha, G. A. C., Salazar, C. A., & Launeau, P. (2012). Using AMS combined with mineral shape preferred orientation analysis to understand the emplacement fabrics of the Apiaí gabbro-norite (Ribeira Belt, SE Brazil). *International Journal of Earth Sciences*, *101*(3), 731–745. https://doi.org/10.1007/s00531-011-0659-x

Armando, G. (1999). Intracontinental alkaline magmatism: Geology, petrography, mineralogy and geochemistry of the Jebel Hayim Massif (central High Atlas-Morocco). *Mémories de Géologie de l'Université de Lausanne*, *31*, 106.

Beauchamp, W. (2004). Superposed folding resulting from inversion of a synrift accommodation zone, Atlas Mountains, Morocco. In K. R. McClay (Ed.), *Thrust tectonics and hydrocarbon systems*, *AAPG Memoir* (Vol. 82, pp. 635–646). AAPG, American Association of Petroleum Geologists.

Biggin, A. J., van Hinsbergen, D. J. J., Langereis, C. G., Straathof, G. B., & Deenen, M. H. L. (2008). Geomagnetic secular variation in the Cretaceous normal superchron and in the Jurassic. *Physics of the Earth and Planetary Interiors*, *169*(1-4), 3–19. https://doi.org/10.1016/j.pepi.2008.07.004

Bouchez, J. L. (1997). Granite is never isotropic: An introduction to AMS studies of granitic rocks. In J. L. Bouchez, D. H. W. Hutton, & W. E. Stephens (Eds.), *Granite: From segregation of melt to emplacement fabrics* (Vol. 8, pp. 95–112). Dordrecht, Netherlands: Springer. https://doi.org/10.1007/978-94-017-1717-5

Bouchez, J.-L. (2000). Anisotropie de susceptibilité magnétique et fabrique des granites. *Comptes Rendus de l'Académie des Sciences - Series IIA - Earth and Planetary Science*, *330*(1), 1–14. https://doi.org/10.1016/S1251-8050(00)00120-8

Bouchez, J. L., & Gleizes, G. (1995). Two-stage deformation of the Mont-Louis-Andorra granite pluton (Variscan Pyrenees) inferred from magnetic susceptibility anisotropy. *Journal of the Geological Society*, *152*(4), 669–679. https://doi.org/10.1144/gsjgs.152.4.0669

Bouchez, J. L., Gleizes, G., Djouadi, T., & Rochette, P. (1990). Microstructure and magnetic susceptibility applied to emplacement kinematics of granites: The example of the Foix pluton (French pyrenees). *Tectonophysics*, *184*(2), 157–171. https://doi.org/10.1016/0040-1951(90)90051-9

Brown, L. L., & McEnroe, S. A. (2015). 916 Ma pole for southwestern Baltica: Palaeomagnetism of the Bjerkreim-Sokndal layered intrusion, Rogaland igneous complex, southern Norway. *Geophysical Journal International*, *203*(1), 567–587. https://doi.org/10.1093/gji/ggv299

Calvín, P., Casas-Sainz, A. M., Villalaín, J. J., & Moussaid, B. (2017). Diachronous folding and cleavage in an intraplate setting (central High Atlas, Morocco) determined through the study of remagnetizations. *Journal of Structural Geology*, *97*, 144–160. https://doi.org/10.1016/j.jsg.2017.02.009

Chadima, M., & Hrouda, F. (2006). Remasoft 3.0 a user-friendly paleomagnetic data browser and analyzer. *Travaux Géophysiques*, *27*, 20–21.

Chadima, M., & Jelinek, V. (2009). Anisoft data browser, 4.2, AGICO inc.

Charrière, A. (1990). *Héritage hercynien et évolution géodynamique alpine d'une chaîne intracontinentale: Le Moyen Atlas au SE de Fès (Maroc)*. Toulouse: Université Paul-Sabatier.

Charrière, A., & Haddoumi, H. (2016). Les <<Couches rouges>> continentales jurassico-crétacées des Atlas marocains (Moyen Atlas, Haut Atlas central et oriental): bilan stratigraphique, paléogéographies successives et cadre géodynamique. *Boletín Geológico y Minero*, *127*(2–3), 407–430.

Day, R., Fuller, M., & Schmidt, V. A. (1977). Hysteresis properties of titanomagnetites: Grain-size and compositional dependence. *Physics of the Earth and Planetary Interiors*, *13*(4), 260–267. https://doi.org/10.1016/0031-9201(77)90108-X

de Sitter, L. U. (1952). Plissement croisé dans le Haut Atlas. *Geologie en Mijnbouw*, *14*, 277–282.

Denyszyn, S. W., Feinberg, J. M., Renne, P. R., & Scott, G. R. (2013). Revisiting the age and paleomagnetism of the Modipe Gabbro of South Africa. *Precambrian Research*, *238*, 176–185. https://doi.org/10.1016/j.precamres.2013.10.002

Dunlop, D. J. (2002). Theory and application of the Day plot (Mrs/Ms versus Hcr/Hc) 1. Theoretical curves and tests using titanomagnetite data. *Journal of Geophysical Research*, *107*(B3), 20562. https://doi.org/10.1029/2001JB000486

Dunlop, D. J., Hyodo, H., Knight, T., & Steele, A. G. (1985). Palaeomagnetism of the Tudor gabbro, Ontario: Evidence for divergence between Grenvillia and interior Laurentia. *Geophysical Journal International*, *83*(3), 699–720. https://doi.org/10.1111/j.1365-246X.1985.tb04333.x

Ebert, Y., Kessel, R., Shaar, R., Agnon, A., & Ron, H. (2010). Petrology and rock magnetism of the gabbro of Troodos ophiolite. *Physics of the Earth and Planetary Interiors*, *183*(3-4), 413–420. https://doi.org/10.1016/j.pepi.2010.09.006

Ettaki, M., Ibouh, H., Chellaï, E. H., & Milhi (2007). Les structures "diapiriques" liasiques du Haut-Atlas central, Maroc: Example de la ride d'Ikerzi. *Africa Geosciences Review*, *14*(1), 79–93.

Evans, M. E., & McElhinny, M. W. (1966). The paleomagnetism of the Modipe Gabbro. *Journal of Geophysical Research*, *71*(24), 6053–6063. https://doi.org/10.1029/JZ071i024p06053

Evans, M. E., McElhinny, M. W., & Gifford, A. C. (1968). Single domain magnetite and high coercivities in a gabbroic intrusion. *Earth and Planetary Science Letters*, *4*(2), 142–146. https://doi.org/10.1016/0012-821X(68)90008-3

Feinberg, J. M., Harrison, R. J., Kasama, T., Dunin-Borkowski, R. E., Scott, G. R., & Renne, P. R. (2006). Effects of internal mineral structures on the magnetic remanence of silicate-hosted titanomagnetite inclusions: An electron holography study. *Journal of Geophysical Research*, *111*, B12S15. https://doi.org/10.1029/2006JB004498.

Feinberg, J. M., Scott, G. R., Renne, P. R., & Wenk, H. R. (2005). Exsolved magnetite inclusions in silicates: Features determining their remanence behavior. *Geology*, *33*(6), 513–516. https://doi.org/10.1130/G21290.1

Ferré, E. C., Bordarier, C., & Marsh, J. S. (2002). Magma flow inferred from AMS fabrics in a layered mafic sill, Insizwa, South Africa. *Tectonophysics*, *354*(1-2), 1–23. https://doi.org/10.1016/S0040-1951(02)00273-1

Fisher, R. (1953). Dispersion on a sphere. *Proceedings of the Royal Society A: Mathematical, Physical and Engineering Sciences*, *217*(1130), 295–305. https://doi.org/10.1098/rspa.1953.0064

Frizon de Lamotte, D., Zizi, M., Missenard, Y., Hadif, M., El Azzouzi, M., Maury, R. C., … Michard, A. (2008). The atlas system. In A. Michard, et al. (Eds.), *Continental evolution: The geology of Morocco. Lecture notes in Earth sciences 116*, (pp. 133–202). Berlin: Springer. https://doi.org/10.1007/978-3-540-77076-3_4

Gil, A., Lago, M., Galé, C., Pocoví, A., & Arranz, E. (2002). Magnetic fabric in folded sills and lava flows. A case study in the Permian basalts of the Anayet Massif (Pyrenean axial zone, Spain). *Tectonophysics*, *350*(1), 1–15. https://doi.org/10.1016/S0040-1951(02)00078-1

Girdler, R. W. (1961). The measurement and computation of anisotropy of magnetic susceptibility of rocks. *Geophysical Journal International*, *5*(1), 34–44. https://doi.org/10.1111/j.1365-246X.1961.tb02927.x

Gradstein, F. M., Ogg, J. G., Schmitz, M. D., & Ogg, G. M. (2012). *The geologic time scale*. Boston: Elsevier.

Granot, R., Tauxe, L., Gee, J., & Ron, H. (2007). A view into the Cretaceous geomagnetic field from analysis of gabbros and submarine glasses. *Earth and Planetary Science Letters*, *256*(1-2), 1–11. https://doi.org/10.1016/j.epsl.2006.12.028

Hailwood, E. A., & Mitchell, J. G. (1971). Palaeomagnetic and radiometric dating results from Jurassic intrusions in South Morocco. *Geophysical Journal International*, *24*(4), 351–364. https://doi.org/10.1111/j.1365-246X.1971.tb02183.x

Hurst, S. D., Verosub, K. L., & Moores, E. M. (1992). Paleomagnetic constraints on the formation of the Solea graben, Troodos ophiolite, Cyprus. *Tectonophysics*, *208*(4), 431–445. https://doi.org/10.1016/0040-1951(92)90439-D

Ibouh, H., Michard, A., Charrière, A., Benkaddour, A., & Rhoujjati, A. (2014). Tectonic–karstic origin of the alleged "impact crater" of Lake Isli (Imilchil district, High Atlas, Morocco). *Comptes Rendus Geoscience*, *346*(3-4), 82–89. https://doi.org/10.1016/j.crte.2014.03.005

Izquierdo-Llavall, E., Román-Berdiel, T., Casas, A. M., Oliva-Urcia, B., Gil-Peña, I., Soto, R., & Jabaloy, A. (2012). Magnetic and structural study of the Eaux-Chaudes intrusion: Understanding the Variscan deformation in the western axial zone (Pyrenees). *International Journal of Earth Sciences*, *101*(7), 1817–1834. https://doi.org/10.1007/s00531-012-0760-9

Jelínek, V. (1978). Statistical processing of anisotropy of magnetic susceptibility measured on groups of specimens. *Studia Geophysica et Geodaetica*, *22*(1), 50–62. https://doi.org/10.1007/BF01613632

Jelinek, V. (1981). Characterization of the magnetic fabric of rocks. *Tectonophysics*, *79*(3-4), 63–67. https://doi.org/10.1016/0040-1951(81)90110-4

Kirschvink, J. L. (1980). The least-squares line and plane and the analysis of paleomagnetic data. *Geophysical Journal of the Royal Astronomical Society*, *62*(3), 699–718. https://doi.org/10.1111/j.1365-246X.1980.tb02601.x

Laville, E., & Piqué, A. (1992). Jurassic penetrative deformation and Cenozoic uplift in the central High Atlas (Morocco): A tectonic model. Structural and orogenic inversions. *Geologische Rundschau*, *81*(1), 157–170. https://doi.org/10.1007/BF01764546

Liodas, N. T., Gébelin, A., Ferré, E. C., & Misgna, G. M. (2013). Deformation coupling between the Archean Pukaskwa intrusive complex and the Hemlo shear zone, Superior Province, Canada. *Tectonophysics*, *608*, 1226–1237. https://doi.org/10.1016/j.tecto.2013.06.022

Lüneburg, C. M., Lampert, S. A., Lebit, H. D., Hirt, A. M., Casey, M., & Lowrie, W. (1999). Magnetic anisotropy, rock fabrics and finite strain in deformed sediments of SW Sardinia (Italy). *Tectonophysics*, *307*(1-2), 51–74. https://doi.org/10.1016/S0040-1951(99)00118-3

Maes, S. M., Tikoff, B., Ferré, E. C., Brown, P. E., & Miller, J. D. Jr. (2007). The Sonju Lake layered intrusion, northeast Minnesota: Internal structure and emplacement history inferred from magnetic fabrics. *Precambrian Research*, *157*(1-4), 269–288. https://doi.org/10.1016/j.precamres.2007.02.021

Mattauer, M., Tapponnier, P., & Proust, F. (1977). Sur les mecanismes de formation des chaines intracontinentales; l'exemple des chaines atlasiques du Maroc. *Bulletin de la Societe Geologique de France*, *S7-XIX*(3), 521–526. https://doi.org/10.2113/gssgfbull.S7-XIX.3.521

McCabe, C., Jackson, M., & Ellwood, B. B. (1985). Magnetic anisotropy in the Trenton limestone: Results of a new technique, anisotropy of anhysteretic susceptibility. *Geophysical Research Letters*, *12*(6), 333–336. https://doi.org/10.1029/GL012i006p00333

McEnroe, S. A. (1996). A Barremian-Aptian (Early Cretaceous) North American paleomagnetic reference pole. *Journal of Geophysical Research: Solid Earth*, *101*(B7), 15,819–15,835. https://doi.org/10.1029/96JB00652

McNulty, B. A., Tobisch, O. T., Cruden, A. R., & Gilder, S. (2000). Multistage emplacement of the Mount Givens pluton, central Sierra Nevada batholith, California. *Geological Society of America Bulletin*, *112*(1), 119–135. https://doi.org/10.1130/0016-7606(2000)112%3C119:MEOTMG%3E2.0.CO;2

Michard, A., Ibouh, H., & Charrière, A. (2011). Syncline-topped anticlinal ridges from the High Atlas: A Moroccan conundrum, and inspiring structures from the Syrian Arc, Israel. *Terra Nova*, *23*(5), 314–323. https://doi.org/10.1111/j.1365-3121.2011.01016.x

Morrish, A. H. (1965). *The physical principles of magnetism*. Hoboken, NJ: John Wiley.

Moussaid, B., Villalaín, J. J., Casas-Sainz, A., El Ouardi, H., Oliva-Urcia, B., Soto, R., … Torres-López, S. (2015). Primary vs. secondary curved fold axes: Deciphering the origin of the Aït Attab syncline (Moroccan High Atlas) using paleomagnetic data. *Journal of Structural Geology*, *70*, 65–77. https://doi.org/10.1016/j.jsg.2014.11.004

Muxworthy, A. R., & Evans, M. E. (2013). Micromagnetics and magnetomineralogy of ultrafine magnetite inclusions in the Modipe Gabbro. *Geochemistry, Geophysics, Geosystems*, *14*, 921–928. https://doi.org/10.1029/2012GC004445

Muxworthy, A. R., Evans, M. E., Scourfield, S. J., & King, J. G. (2013). Paleointensity results from the late-Archaean Modipe Gabbro of Botswana. *Geochemistry, Geophysics, Geosystems*, *14*, 2198–2205. https://doi.org/10.1002/ggge.20142

O'Driscoll, B., Stevenson, C. E. T. E., Troll, V. R., Trolly, V. R., & Troll, V. R. (2008). Mineral lamination development in layered gabbros of the British Palaeogene igneous province: A combined anisotropy of magnetic susceptibility, quantitative textural and mineral chemistry study. *Journal of Petrology*, *49*(6), 1187–1221. https://doi.org/10.1093/petrology/egn022

Oliva-Urcia, B., Casas, A. M., Pueyo, E. L., Juan, A., Oliva-Urcía, B., Pueyo, E. L., … Pocovi-Juan, A. (2012). Paleomagnetic evidence for non-rotational kinematics of the South Pyrenean Frontal Thrust at the western termination of the External Sierras southwestern central. *Geologica Acta*, *10*, 125–144. https://doi.org/10.1344/105.000001704

Oliva-Urcia, B., Casas, A. M., Soto, R., Villalaín, J. J., & Kodama, K. (2011). A transtensional basin model for the Organyà basin (central southern Pyrenees) based on magnetic fabric and brittle structures. *Geophysical Journal International*, *184*(1), 111–130. https://doi.org/10.1111/j.1365-246X.2010.04865.x

Osete, M. L., Rey, D., Villalaín, J. J., & Juárez, M. (1997). The Late Carboniferous to Late Triassic segment of the apparent polar wander path of Iberia. *Geologie En Mijnbouw (Geology and Mining)*, *76*(1/2), 105–119. https://doi.org/10.1023/A:1003197500052

Pariso, J. E., Kelso, P., & Richter, C. (1996). Paleomagnetism and rock magnetic properties of gabbro from Hole 894G, Hess Deep. Proceedings of the Ocean Drilling. Program, 147 Scientific Results. Ocean Drilling Program. https://doi.org/10.2973/odp.proc.sr.147.023.1996

Poisson, A., Hadri, M., Milhi, A., Julien, M., & Andrieux, J. (1998). The Central High-Atlas (Morocco). Litho- and chrono-stratigraphic correlations during Jurassic times between Tinjdad and Tounfite. Origin of subsidence. In S. Crasquin-Soleau & E. Barrier (Eds.), *Peri-Tethys memoir 4: Epicratonic basins of Peri-Tethyan platforms* (pp. 237–256). Paris: Mémoires du Muséum National d'Histoire Naturelle.

Potter, D. K., & Stephenson, A. (1988). Single-domain particles in rocks and magnetic fabric analysis. *Geophysical Research Letters*, *15*(10), 1097–1100. https://doi.org/10.1029/GL015i010p01097

Pueyo Anchuela, Ó., Gil Imaz, A., Gil-Peña, I., Maestro, A., Galindo-Zaldivar, J., López-Martínez, J., … Oliva-Urcia, B. (2014). Application of AMS for reconstruction of the geological evolution of recent volcanic systems: Case of Deception Island (South Shetland Islands, Antarctica). *Tectonophysics*, *626*, 69–85. https://doi.org/10.1016/j.tecto.2014.03.032

Renne, P. R., Scott, G. R., Glen, J. M. G., & Feinberg, J. M. (2002). Oriented inclusions of magnetite in clinopyroxene: Source of stable remanent magnetization in gabbros of the Messum Complex, Namibia. *Geochemistry, Geophysics, Geosystems*, *3*(12), 1079. https://doi.org/10.1029/2002GC000319

Román-Berdiel, T. (1999). Geometry of granite emplacement in the upper crust: Contributions of analogue modelling. *Geological Society, London, Special Publications*, *168*(1), 77–94. https://doi.org/10.1144/GSL.SP.1999.168.01.06

Román-Berdiel, T., Casas, A., Oliva-Urcia, B., Pueyo, E., & Rillo, C. (2004). The main Variscan deformation event in the Pyrenees: New data from the structural study of the Bielsa granite. *Journal of Structural Geology*, *26*(4), 659–677. https://doi.org/10.1016/j.jsg.2003.09.001

Román-Berdiel, T., Casas, A. M., Oliva-Urcia, B., Pueyo, E. L., Liesa, C., & Soto, R. (2006). The Variscan Millares granite (central Pyrenees): Pluton emplacement in a T fracture of a dextral shear zone. *Geodinamica Acta*, *19*(3-4), 197–211. https://doi.org/10.3166/ga.19.197-211

Roman-Berdiel, T., Gapais, D., & Brun, J. P. (1995). Analogue models of laccolith formation. *Journal of Structural Geology*, *17*(9), 1337–1346. https://doi.org/10.1016/0191-8141(95)00012-3

Roman-Berdiel, T., Gapais, D., & Brun, J.-P. (1997). Granite intrusion along strike-slip zones in experiment and nature. *American Journal of Science*, *297*(6), 651–678. https://doi.org/10.2475/ajs.297.6.651

Saura, E., Vergés, J., Martín-Martín, J. D., Messager, G., Moragas, M., Razin, P., … Hunt, D. W. (2014). Syn- to post-rift diapirism and minibasins of the central High Atlas (Morocco): The changing face of a mountain belt. *Journal of the Geological Society*, *171*(1), 97–105. https://doi.org/10.1144/jgs2013-079

Schöbel, S., & de Wall, H. (2014). AMS-NRM interferences in the Deccan basalts: Toward an improved understanding of magnetic fabrics in flood basalts. *Journal of Geophysical Research: Solid Earth*, *119*, 2651–2678. https://doi.org/10.1002/2013JB010660

Schofield, N., Alsop, I., Warren, J., Underhill, J. R., Lehne, R., Beer, W., & Lukas, V. (2014). Mobilizing salt: Magma-salt interactions. *Geology*, *42*(7), 599–602. https://doi.org/10.1130/G35406.1

Schöpa, A., Floess, D., Blanquat, M., Saint, D., Annen, C., & Launeau, P. (2015). The relation between magnetite and silicate fabric in granitoids of the Adamello batholith. *Tectonophysics*, *642*, 1–15. https://doi.org/10.1016/j.tecto.2014.11.022

Spera, F. (1980). Thermal evolution of plutons: A parameterized approach. *Science (New York, N.Y.)*, *207*(4428), 299–301. https://doi.org/10.1126/science.207.4428.299

Tarling, D. H., & Hrouda, F. (1993). *The magnetic anisotropy of rocks*. London: Chapman & Hall.

Teixell, A., Arboleya, M.-L., Julivert, M., & Charroud, M. (2003). Tectonic shortening and topography in the central High Atlas (Morocco). *Tectonics*, *22*(5), 1051. https://doi.org/10.1029/2002TC001460

Torres-López, S., Casas, A. M., Villalaín, J. J., El Ouardi, H., & Moussaid, B. (2016). Pre-Cenomanian vs. Cenozoic folding in the High Atlas revealed by palaeomagnetic data. *Terra Nova*, *28*(2), 110–119. https://doi.org/10.1111/ter.12197

Torres-López, S., Villalaín, J. J., Casas, A. M., El Ouardi, H., Moussaid, B., & Ruiz-Martínez, V. C. (2014). Widespread Cretaceous secondary magnetization in the High Atlas (Morocco). A common origin for the Cretaceous remagnetizations in the western Tethys? *Journal of the Geological Society*, *171*(5), 673–687. https://doi.org/10.1144/jgs2013-107

Torsvik, T. H., Van der Voo, R., Preeden, U., Niocaill, C. M., Steinberger, B., Doubrovine, P. V., … Cocks, L. R. M. (2012). Phanerozoic polar wander, palaeogeography and dynamics. *Earth-Science Reviews*, *114*(3-4), 195–217. https://doi.org/10.1016/j.earscirev.2012.06.002

Usui, Y., Nakamura, N., & Yoshida, T. (2006). Magnetite microexsolutions in silicate and magmatic flow fabric of the Goyozan granitoid (NE Japan): Significance of partial remanence anisotropy. *Journal of Geophysical Research*, *111*, B11101. https://doi.org/10.1029/2005JB004183

Usui, Y., Shibuya, T., Sawaki, Y., & Komiya, T. (2014). Rock magnetism of tiny exsolved magnetite in plagioclase from a Paleoarchean granitoid in the Pilbara craton. *Geochemistry, Geophysics, Geosystems*, *16*, 112–125. https://doi.org/10.1002/2014GC005508

Usui, Y., & Yamazaki, S. (2010). Salvaging primary remanence from hydrothermally altered oceanic gabbros in the Oman ophiolite: A selective destructive demagnetization approach. *Physics of the Earth and Planetary Interiors*, *181*(1-2), 1–11. https://doi.org/10.1016/j.pepi.2010.04.008

Van der Voo, R. (1967). The rotation of Spain: Palaeomagnetic evidence from the Spanish meseta. *Palaeogeography, Palaeoclimatology, Palaeoecology*, *3*, 393–416. https://doi.org/10.1016/0031-0182(67)90027-2

Van der Voo, R. (1969). Paleomagnetic evidence for the rotation of the Iberian Peninsula. *Tectonophysics*, *7*(1), 5–56. https://doi.org/10.1016/0040-1951(69)90063-8

Verwey, E. J. (1939). Electronic conduction of magnetite (Fe_3O_4) and its transition point at low temperatures. *Nature (London)*, *144*(3642), 327–328. https://doi.org/10.1038/144327b0

Villalaín, J., Fernández-González, G., Casas, A. M., & Gil-Imaz, A. (2003). Evidence of a cretaceous remagnetization in the Cameros Basin (North Spain): Implications for basin geometry. *Tectonophysics*, *377*(1-2), 101–117. https://doi.org/10.1016/j.tecto.2003.08.024

Villalaín, J. J., Casas-Sainz, A. M., & Soto, R. (2016). Reconstruction of inverted sedimentary basins from syn-tectonic remagnetizations. A methodological proposal. *Geological Society, London, Special Publications*, *425*(1), 233–246. https://doi.org/10.1144/SP425.10

Villalaín, J. J., Ruiz, V. C., Torres-López, S., Casas-Sainz, A., Moussaid, B., & Calvín, P. (2016). Estudio paleomagnético preliminar de diques mesozoicos del Alto Atlas. Control térmico en la generación de pirrotina en calizas remagnetizadas con magnetita. In J. A. Morales-González, et al. (Eds.), *IX Congreso Geológico de España* (Vol. 16, pp. 901–904). Huelva, Spain: Sociedad Geológica de España.

Walz, F. (2002). The Verwey transition—A topical review. *Journal of Physics: Condensed Matter*, *14*(12), R285–R340. https://doi.org/10.1088/0953-8984/14/12/203

Wenk, H.-R., Chen, K., & Smith, R. (2011). Morphology and microstructure of magnetite and ilmenite inclusions in plagioclase from Adirondack anorthositic gneiss. *American Mineralogist*, *96*(8-9), 1316–1324. https://doi.org/10.2138/am.2011.3760

Zayane, R., Essaifi, A., Maury, R. C., Piqué, A., Laville, E., & Bouabdelli, M. (2002). Cristallisation fractionnée et contamination crustale dans la série magmatique jurassique transitionnelle du Haut Atlas central (Maroc). *Comptes Rendus Geoscience*, *334*(2), 97–104. https://doi.org/10.1016/S1631-0713(02)01716-9